

Excited states, symmetry breaking, and unphysical solutions in state-specific CASSCF theory

Antoine Marie^{1,2} and Hugh G. A. Burton^{1, a)}

¹⁾Physical and Theoretical Chemical Laboratory, Department of Chemistry, University of Oxford, Oxford, OX1 3QZ, U.K.

²⁾Current address: Laboratoire de Chimie et Physique Quantiques (UMR 5626), Université de Toulouse, CNRS, UPS, Toulouse, France

(Dated: 27 January 2023)

State-specific electronic structure theory provides a route towards balanced excited-state wave functions by exploiting higher-energy stationary points of the electronic energy. Multiconfigurational wave function approximations can describe both closed- and open-shell excited states and avoid the issues associated with state-averaged approaches. We investigate the existence of higher-energy solutions in complete active space self-consistent field (CASSCF) theory and characterise their topological properties. We demonstrate that state-specific approximations can provide accurate higher-energy excited states in H₂ (6-31G) with more compact active spaces than would be required in a state-averaged formalism. We elucidate the unphysical stationary points, demonstrating that they arise from redundant orbitals when the active space is too large, or symmetry breaking when the active space is too small. Furthermore, we investigate the conical intersection in CH₂ (6-31G) and the avoided crossing in LiF (6-31G), revealing the severity of root flipping and demonstrating that state-specific solutions can behave quasi-diabatically or adiabatically. These results elucidate the complexity of the CASSCF energy landscape, highlighting the challenges faced by practical state-specific calculations.

I. Introduction

Electronic excited states are fundamentally higher-energy solutions to the time-independent Schrödinger equation. “State-specific” representations can be identified using higher-energy stationary points of the electronic energy landscape.¹ The exact excited states in full configuration interaction (FCI) correspond to energy saddle points and the number of downhill Hessian eigenvalues increases with each energy level.^{1–7} Higher-energy stationary points also exist in non-linear wave function approximations, but the development of practical state-specific methods has been hindered by the challenges of non-ground-state optimisation, the non-linearity of the electronic energy landscape, and the presence of unphysical solutions.

Instead, the workhorse of modern excited-state electronic struture theory is linear-response time-dependent density functional theory (LR-TDDFT), which predicts excitation energies from the response of the ground-state electron density to a weak external perturbation.^{8–10} Despite its computational efficiency, LR-TDDFT inherits the failures of approximate Kohn-Sham (KS) exchange-correlation functionals, creating large errors for bond dissociation or open-shell electronic states.¹¹ Furthermore, the ubiquitous adiabatic approximation excludes double excitations and their associated avoided crossings.^{10,12} Alternative single-reference methods such as algebraic diagrammatic construction^{13,14} (ADC) and equation-of-motion coupled cluster^{15,16} (EOM-CC) can provide more accurate excitation energies at a greater computational cost, but depend strongly on the quality of the reference determinant. The strong influence of the ground-state orbitals can also create an unbalanced description of charge transfer and Rydberg excitations,^{17,18} where significant electronic relaxation can occur.^{19–24}

These challenges have encouraged researchers to revisit excited state-specific approximations. For higher-energy SCF

calculations (Δ SCF), this progress has been catalysed by the development of new optimisation algorithms that avoid variational collapse to the ground state, including the maximum overlap method,^{25–27} square-gradient optimisation,^{28,29} state-targeted energy projection,³⁰ quasi-Newton direct orbital optimisation,^{31–33} and generalised variational principles.³⁴ Recent calculations have shown that higher-energy Hartree-Fock (HF) and KS-DFT solutions can accurately describe charge transfer and double excitations at a low computational cost.^{25,29} Beyond SCF approximations, higher-energy variational or projective coupled-cluster (Δ CC) solutions can provide more accurate double and double core excitations by incorporating dynamic electron correlation.^{35–41} While Δ SCF and Δ CC are successful for double and charge transfer excitations, these single-reference methods cannot describe open-shell excited states and statically correlated ground states. The onset of this failure usually becomes apparent through spin contamination,^{42,43} spontaneous symmetry breaking,^{11,26,44–48} and additional unphysical solutions.^{35–38,40–42} Furthermore, the solutions of interest can disappear as the molecular structure changes, creating discontinuous excited state energy surfaces or gradients.^{41,42,49–53}

Multiconfigurational SCF (MCSCF) methods,⁵⁴ particularly the complete-active space self-consistent field (CASSCF) formulation,^{55–57} are the state-of-the-art for describing statically correlated electronic systems.⁵⁸ The CASSCF wave function is a linear expansion of all the configurations that can be constructed from a set of partially occupied “active orbitals”, and the energy is optimised with respect to the configuration interaction (CI) and orbital coefficients simultaneously.⁵⁶ It has long been known that higher-energy MCSCF solutions can represent electronic excited states,^{59–64} and that multiple symmetry-broken CASSCF solutions can occur for an inadequate active space.^{65,66} More recently, MCSCF expansions truncated to single excitations have shown promise for singly excited charge transfer states,^{67–71} while state-specific configuration interaction with higher degrees of truncation can han-

^{a)}Electronic mail: hgarburton@gmail.com

dle challenging multireference problems, singly-, and doubly-excited states.⁷² However, the strong coupling between the orbital and CI degrees of freedom makes the optimisation challenging, and it was not until the development of second-order optimisation algorithms that excited-state MCSCF calculations could be performed in practice.^{73–86}

Extensive research in the 1980s focused on characterising higher-energy MCSCF solutions. It was originally suggested that an n th excited state approximation should be the n th state in the configuration expansion.⁷⁶ However, this requirement is often not achieved in practice, resulting in “root flipping”.^{2,59,78} Furthermore, several stationary points satisfying this condition can often be identified.^{3,5,87} The enormous complexity of the multiconfigurational solution space led Golab *et al.* to conclude that “selecting an MCSCF stationary point is a very severe problem.”³ Instead, the state-averaged (SA) approach is generally used, where a weighted average energy of the n lowest CI states constructed from one set of orbitals is optimised.⁷⁸ While this approach has become the method of choice for excited-state CASSCF, it has several disadvantages: discontinuities can occur on the SA-CASSCF potential energy surface if two states require orbitals with significantly different character,⁸⁸ the number of states is limited by the size of the active space; large active spaces are required to target high-lying states; and the Helmann-Feynman theorem cannot be applied to compute nuclear gradients because individual SA-CASSCF solutions are not stationary points of the energy.

Recently, the limitations of SA-CASSCF and the development of non-ground-state SCF optimisation algorithms has inspired several new investigations into state-specific CASSCF excited states. In particular, Neuscamman and co-workers have developed generalized variational principles^{89,90} and the WT approach inspired by MOM-SCF,⁹¹ demonstrating that the issues of root flipping and variational collapse to the ground state can be successfully avoided. Despite these advances, we still do not have a complete understanding of the multiple stationary points on the SS-CASSCF energy landscape and several practical questions remain. For example, how many stationary points are there and how does this change with the active space or basis set size? Where do unphysical solutions arise, what are their characteristics, and when does symmetry breaking occur? And finally, do state-specific excitations behave diabatically or adiabatically as the molecular structure evolves?

Our aim in this work is to answer these questions and establish a theoretical foundation for practical excited state-specific calculations. Using second-order optimisation techniques, we investigate the existence and properties of multiple CASSCF solutions in typical molecular systems. Our numerical optimisation exploits analytic gradients and second derivatives of the CASSCF energy, and the relevant differential geometry is summarised below. Using these techniques, we comprehensively enumerate the multiple CASSCF solutions in H₂ (6-31G) and characterise the resulting unphysical solutions. We find that state-specific calculations can accurately describe high-lying excitations with fewer active orbitals than state-averaged formalisms, and reveal that multiple solutions can arise from active spaces that are too large or too small. We then investigate the conical intersection in CH₂ (6-31G) and the avoided cross-

ing of LiF (6-31G), demonstrating the importance and difficulty of selecting the correct physical solution.

II. Exploring the multiconfigurational energy landscape

A. Defining the CASSCF wave function

A multiconfigurational wave function is defined as the linear combination of M Slater determinants

$$|\Psi_k\rangle = \sum_{I=1}^M C_{Ik} |\Phi_I\rangle, \quad (1)$$

where $|\Phi_I\rangle$ represents different configurations built from a common set of molecular orbitals (MO) $\phi_p(x)$ and the C_{Ik} are the variable CI coefficients for state k .⁹² Here, $x = (r, \sigma)$ is the combined spatial and spin electronic coordinate. The MOs are constructed as linear combinations of n (nonorthogonal) atomic orbitals (AO) $\chi_\mu(x)$ as

$$\phi_p(x) = \sum_{\mu} \chi_{\mu}(x) c_{\cdot p}^{\mu}, \quad (2)$$

where we use the nonorthogonal tensor notation of Ref. 93 and the $c_{\cdot p}^{\mu}$ denote the variable MO coefficients. Normalisation of the wave function, and orthogonalisation of the MOs, is guaranteed by the constraints

$$\sum_{I=1}^M |C_I|^2 = 1 \quad \text{and} \quad \sum_{\mu=1}^n (c^*)_{\cdot p}^{\mu} \langle \chi_{\mu} | \chi_{\nu} \rangle c_{\cdot q}^{\nu} = \delta_{pq}, \quad (3)$$

where $\langle \chi_{\mu} | \chi_{\nu} \rangle$ denotes the AO overlap matrix elements. We will only consider wave functions where C_{Ik} and $c_{\cdot p}^{\mu}$ are real.

When every electronic configuration for a finite basis set is included in an FCI expansion, the global minimum on the parametrised electronic energy landscape corresponds to the exact ground state.¹ Excited states form saddle points of the energy and the number of downhill directions increases with each excitation.^{1,3,6,7} The FCI wave function is invariant to unitary transformations of the MOs, but the number of configurations scales exponentially with the system size.

The complete active space (CAS) framework builds a truncated expansion using every configuration within a set of “active orbitals” that describe the dominant static electron correlation.⁵⁶ The orbitals are partitioned into inactive and virtual orbitals that are doubly occupied or empty in every configuration, respectively, and active orbitals with varying occupations. Simultaneously optimising the energy with respect to the orbital and CI coefficients leads to the state-specific CASSCF approach and gives true stationary points of the electronic energy.^{56,57,77} If the CASSCF wave function targeting the k th excited state is represented by the k th eigenstate of the corresponding CAS-CI expansion, then the Hylleraas-Undheim-MacDonald theorem^{94,95} also provides a upper bound to the excited-state energy.³

B. Differential geometry of the CASSCF energy

We exploit an exponential form of the CASSCF wave function that conserves the orthogonality constraints [Eq. (3)].^{73,75}

Starting from an initial CASSCF wave function $|\Psi_0\rangle$, an arbitrary step can be defined using unitary transformations as

$$|\Psi\rangle = e^{\hat{R}} e^{\hat{S}} |\Psi_0\rangle, \quad (4)$$

where $e^{\hat{R}}$ and $e^{\hat{S}}$ account for orbital relaxation and transformations of the CI component, respectively. The \hat{R} operator is anti-Hermitian and is defined using the second-quantised creation and annihilation operators for the current MOs as^{73,96}

$$\hat{R} = \sum_{p>q} R_{pq} \hat{E}_{pq}^-, \quad (5)$$

where the spin-adapted one-body replacement operators are⁹²

$$\hat{E}_{pq}^- = \sum_{\sigma \in \{\uparrow, \downarrow\}} \hat{a}_{q\sigma}^\dagger \hat{a}_{p\sigma} - \hat{a}_{p\sigma}^\dagger \hat{a}_{q\sigma}. \quad (6)$$

The invariance of the energy with respect to inactive-inactive, active-active, and virtual-virtual orbital transformations means that R_{pq} can be further restricted to only excitations between different sub-blocks. Similarly, $e^{\hat{S}}$ performs a unitary transformation between the CI component of $|\Psi_0\rangle$ and the remaining orthogonal states $|\Psi_K\rangle$ in the current CASCI space, with \hat{S} defined as⁷⁵

$$\hat{S} = \sum_{K \neq 0} S_K (|\Psi_K\rangle \langle \Psi_0| - |\Psi_0\rangle \langle \Psi_K|). \quad (7)$$

Using the exponential parametrisation, the CASSCF energy can be expressed as

$$E(\mathbf{R}, \mathbf{S}) = \langle \Psi_0 | e^{-\hat{S}} e^{-\hat{R}} \hat{H} e^{\hat{R}} e^{\hat{S}} | \Psi_0 \rangle, \quad (8)$$

where \mathbf{R} and \mathbf{S} are vectors that gather the R_{pq} and S_K coefficients in the orbital and CI transformations, respectively, and \hat{H} is the electronic Hamiltonian. Stationary points of E , corresponding to optimal CASSCF solutions, then occur when the gradients with respect to orbital and CI transformations are simultaneously zero. Performing a Baker–Campbell–Hausdorff expansion of the energy to second order gives⁷⁵

$$\begin{aligned} E \approx & \langle \Psi_0 | \hat{H} | \Psi_0 \rangle + \langle \Psi_0 | [\hat{H}, (\hat{R} + \hat{S})] | \Psi_0 \rangle \\ & + \frac{1}{2} \langle \Psi_0 | [[\hat{H}, (\hat{R} + \hat{S})], (\hat{R} + \hat{S})] | \Psi_0 \rangle + \dots \end{aligned} \quad (9)$$

Expressions for the first- and second-derivatives of the energy can then be identified as

$$\left. \frac{\partial E}{\partial R_{pq}} \right|_{\mathbf{R}, \mathbf{S}=\mathbf{0}} = \langle \Psi_0 | [\hat{H}, \hat{E}_{pq}^-] | \Psi_0 \rangle, \quad (10a)$$

$$\left. \frac{\partial E}{\partial S_K} \right|_{\mathbf{R}, \mathbf{S}=\mathbf{0}} = 2 \langle \Psi_0 | \hat{H} | \Psi_K \rangle, \quad (10b)$$

and

$$\left. \frac{\partial^2 E}{\partial R_{pq} \partial R_{rs}} \right|_{\mathbf{R}, \mathbf{S}=\mathbf{0}} = \frac{1}{2} (1 + P_{pq,rs}) \langle \Psi_0 | [[\hat{H}, \hat{E}_{pq}^-], \hat{E}_{rs}^-] | \Psi_0 \rangle, \quad (11a)$$

$$\left. \frac{\partial^2 E}{\partial R_{pq} \partial S_K} \right|_{\mathbf{R}, \mathbf{S}=\mathbf{0}} = \langle \Psi_0 | [\hat{H}, \hat{E}_{pq}^-] | \Psi_K \rangle, \quad (11b)$$

$$\left. \frac{\partial E}{\partial S_L \partial S_K} \right|_{\mathbf{R}, \mathbf{S}=\mathbf{0}} = 2 \langle \Psi_K | \hat{H} - E_0 | \Psi_L \rangle, \quad (11c)$$

where E_0 is the energy at $\mathbf{R}, \mathbf{S} = \mathbf{0}$, $P_{pq,rs}$ permutes the (pq) and (rs) indices, and the Hermiticity of \hat{H} and $[\hat{H}, \hat{E}_{pq}^-]$ have been exploited. Explicit formulae for these expressions have been summarised elsewhere [see Ref. 4] but are given in the Appendix A for completeness.

Note that the first and second derivatives can only be computed when $\mathbf{R} = \mathbf{0}$ and $\mathbf{S} = \mathbf{0}$.⁹⁶ Therefore, after taking a step in the parameter space, the energy gradient and Hessian must be computed using the new MOs and CI vectors corresponding to the updated wave function. A similar shift in the reference state after each step is also required for second-order HF optimisation algorithms.^{42,97}

C. Characterising distinct solutions

The invariance to unitary transformations within each orbital partition means that the same CASSCF wave function can be identified with different CI or MO coefficients. We use the overlap between two stationary solutions $|^x\Psi\rangle$ and $|^w\Psi\rangle$ to define a positive semidefinite distance metric

$$d(x, w) = 1 - |\langle ^x\Psi | ^w\Psi \rangle|. \quad (12)$$

The overlap for two arbitrary CI wave functions with M_x and M_w configurations, respectively, is given by

$$\langle ^x\Psi | ^w\Psi \rangle = \sum_{I=1}^{M_x} \sum_{J=1}^{M_w} {}^xC_I^* \langle {}^x\Phi_I | {}^w\Phi_J \rangle {}^wC_J. \quad (13)$$

Since $|^x\Psi\rangle$ and $|^w\Psi\rangle$ have different sets of MOs, evaluating the overlap matrix elements $\langle {}^x\Phi_I | {}^w\Phi_J \rangle$ requires a nonorthogonal framework. We compute these matrix elements using the extended nonorthogonal Wick's theory,^{98,99} which avoids the computationally expensive generalized Slater–Condon rules.¹⁰⁰

To understand the MOs in a CASSCF solution, we canonicalise the inactive and virtual orbitals and construct natural orbitals within the active space. The canonical inactive and virtual orbitals, and their associated orbital energies, are identified by diagonalising the relevant sub-blocks of the generalized Fock matrix,¹⁰¹ defined as

$$F_{pq} = \sum_r \gamma_{pr} h_{rq} + \sum_{rst} \Gamma_{prst} (qr|st). \quad (14)$$

Here, γ_{pq} and Γ_{prst} are the one- and two-body reduced density matrix elements in the MO basis, h_{rq} are the one-electron Hamiltonian matrix elements, and $(qr|st)$ are the two-electron repulsion integrals. The natural orbitals within the active space are the eigenvectors of the one-body reduced density matrix and their eigenvalues are the occupation numbers n_p .¹⁰²

D. Optimization techniques

Since we are concerned with understanding the CASSCF solution space, we require an algorithm capable of converging arbitrary stationary points on the energy landscape, including minima and higher-index saddle points. Higher-energy

CASSCF stationary points are notoriously difficult to converge due to the strong coupling between the orbital and CI degrees of freedom,^{59,63,64,75,80} and the possibility of root flipping in the configuration space.^{78,103} Therefore, we employ second-order techniques that introduce the orbital-CI coupling through the analytic Hessian matrix of second derivatives. These algorithms are too computationally expensive to be practical for real systems, but they are sufficient for understanding the CASSCF solutions in small molecules.

We search for multiple solutions using several initial guesses generated using random orbital and CI rotations from the ground state HF solution. The eigenvector-following technique with analytic gradient and Hessian information was used to target stationary points with a particular Hessian index.^{104,105} While this method has been described in detail elsewhere [see Ref. 106], we include a summary in Appendix B. Related mode-following methods have previously been applied to locate higher-energy electronic stationary points in multiconfigurational^{2–4,107} and single-determinant⁴² SCF calculations. The convergence behaviour was further improved with a modified trust region approach based on the dogleg method.¹⁰⁸ Trust region methods are a well-established approach for controlling the convergence of second-order methods in CASSCF calculations.^{80–83} Once a set of stationary points have been identified, their evolution with changes in the molecular structure can be determined by using the optimised orbital and CI coefficients at one geometry to define an initial guess at the next geometry. Since the Hessian index may not be conserved along a reaction coordinate,² these subsequent calculations are performed using a trust region Newton–Raphson algorithm [Appendix C].

We have implemented this numerical optimisation in an extension to the PySCF software package.¹⁰⁹ The convergence threshold for the root-mean-squared value of the gradient amplitudes was universally set to 10^{-8} E_h. The canonical and natural orbitals for stationary points were subsequently computed using PySCF and visualised using VMD.¹¹⁰ All other graphical figures were created using Mathematica 12.0.¹¹¹

III. Results and Discussion

A. Molecular H₂ dissociation

We start by considering the H₂ binding curve using the 6-31G basis set.¹¹² To identify all the CASSCF(2,2) solutions, a comprehensive search was performed using up to 1000 random starting points for target Hessian indices from 0 to 16. Solutions were identified near the equilibrium geometry $R = 1.0 a_0$ and the dissociation limit $R = 6.0 a_0$, and were then traced over all bond lengths, as shown in Fig. 1. We believe that we have found every stationary points on the landscape, although the nature of non-convex optimisation means that this can never be guaranteed. To the best of our knowledge, this study is the first comprehensive enumeration of the CASSCF solutions for a molecular system.

1. Excitations near equilibrium

Near the equilibrium geometry, the ground state of H₂ can be accurately described using a single reference approximation.

We have identified 25 stationary points on the CASSCF(2,2) energy landscape, corresponding to 19 singlet solutions and 6 triplet solutions (Table I). Each of the exact FCI states has

TABLE I: Energies of H₂ at $R = 1 a_0$ using the 6-31G basis set for various formalism: FCI, SA-CASSCF(2,2), SA-CASSCF(3,2), and SS-CASSCF(2,2).

State	FCI	SA(2,2)	SA(3,2)	SS(2,2)	$\langle S^2 \rangle$	Index
0	-1.09897	-1.07170	-1.08924	-1.09225	0	0
				-1.08569	0	1
				-1.07871	0	2
1	-0.57616	-0.57166	-0.57406	-0.57417	2	1
2	-0.46395	-0.43494	-0.44196	-0.46368	0	2
3	-0.28180		-0.27990	-0.27990	2	2
4	-0.07450		-0.06164	-0.05946	0	3
5	0.32015	0.33066	0.32624	0.31914	0	3
				0.31821	0	2
				0.31844	0	2
				0.32440	0	3
6	0.51519		0.51654	0.51638	2	3
7	0.57224		0.61682	0.61429	0	4
8	0.62520			0.62401	2	3
9	0.86353		0.86876	0.86392	0	5
				0.85673	0	4
				0.86266	0	4
10	0.96373			0.91147	0	4
11	1.30761			1.30572	2	4
12	1.46479			1.45704	0	5
13	1.61884			1.61685	2	5
14	1.81277			1.80747	0	6
15	2.71948			2.71766	0	7
				2.70046	0	6
				2.69883	0	5

a corresponding SS-CASSCF(2,2) counterpart, and the energetic agreement between these solutions is consistent for all excitations. We have also found several additional solutions that appear to be less accurate approximations to the exact states, which will be characterised in Sections III A 2 and III A 3. In comparison, the SA-CASSCF(2,2) approach can only describe the lowest triplet and the three lowest singlet states, while increasing the number of active orbitals to a (3,2) active space provides an approximation to the lowest nine excitations.

These results demonstrate two important features of state-specific calculations. Firstly, they can describe more excited states than state-averaged calculations by defining the active space using only orbitals that are relevant for a particular excitation. This property allows higher energy excitations to be predicted while avoiding large active spaces and the associated increase in the configuration space.³ Although more accurate energies are generally preferred even if they are not variational. Secondly, bespoke orbital optimisation for each state-specific solutions can give more accurate total energies for the excited states compared to the state-averaged approach. For example, the mean absolute deviations (MAD) for the lowest four states are 2.5 mE_h and 17.8 mE_h for the state-specific and state-

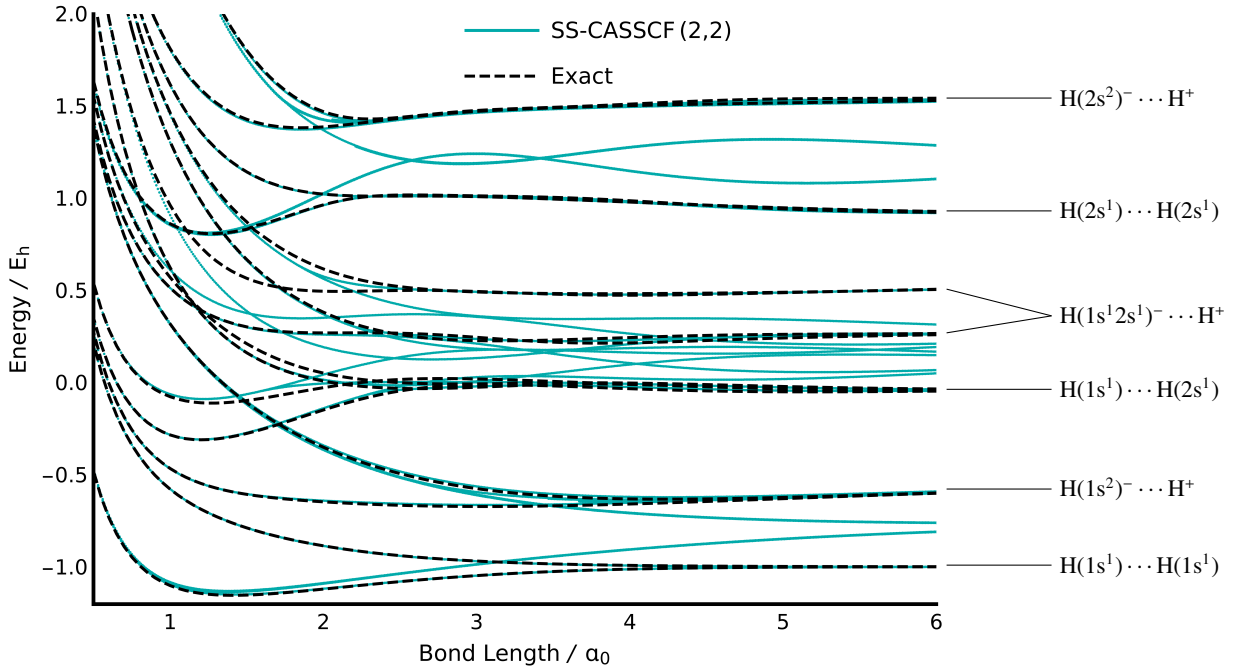


FIG. 1: State-specific CASSCF(2,2) stationary points can be identified for every excited FCI state in H_2 . Additional solutions can also be found that dissociate to an unphysical electronic state.

averaged CASSCF(2,2) approaches, respectively.

Using analytic second derivatives of the energy also allows the nature of SS-CASSCF(2,2) stationary points to be characterised according to their number of downhill directions. The corresponding Hessian index for each solution is listed in Table I. It is known that the exact n -th excited state should have n downhill directions.^{1,2,4} We find that the SS-CASSCF(2,2) excited states are all saddle points on the electronic energy landscape and the Hessian index generally increases with the energy, in common with the observations for other theoretical approximations.^{25,28,40,42} However, except for the lowest three exact states, the Hessian index does not provide a reliable indicator of the corresponding exact excitation index. This mismatch must always occur for higher-lying excited states as the approximate CASSCF(2,2) wave function has fewer degrees of freedom than the exact formulation. Consequently, if we only consider stationary points of the correct Hessian index, then we must forgo the advantages of capturing state-specific excitations outside the state-averaged active space.

2. Multiple ground state solutions

While Table I shows that a SS-CASSCF(2,2) approximation can be identified for each exact eigenstate, we also find additional state-specific solutions. In particular, there are three close-lying stationary points that can be considered as approximations to the ground state, with Hessian indices of 0, 1, and 2 in order of ascending energy. This pattern of multiple solutions is repeated for the $(2\sigma_g)^2$ and $(2\sigma_u)^2$ singlet configurations, while the other closed-shell $(1\sigma_g)^2$ configuration exhibits four close-lying solutions. Choosing the most physical solution for each eigenstate presents a challenge for state-specific CASSCF

approaches. Therefore, it is important that we understand their mathematical origins and physical differences.

The natural orbitals in the active space provides a clear explanation for the multiple H_2 ground-state solutions. Figure 2A compares the natural orbitals and occupation numbers for the three lowest-energy singlet stationary points. Since the ground state at the equilibrium geometry can be relatively well approximated by a single closed-shell Slater determinant, the active space for each of these solutions includes a $(1\sigma_g)$ -like natural orbital that is almost completely doubly occupied. This natural orbital dominates the electronic wave function and the corresponding energies are all relatively close approximations to the exact ground state. However, the second active orbital, which is almost completely unoccupied, is different for each solutions, corresponding to a $(1\sigma_u)$, $(2\sigma_g)$, or $(2\sigma_u)$ orbital as the energy increases, respectively. These higher-energy stationary points have downhill orbital rotations that interconvert the multiple ground state solutions and correspond to the negative eigenvalues of the Hessian.

Different choices for the nearly unoccupied active orbital have only a small effect on the total H_2 energy near equilibrium. However, the incorrect choice of the active space becomes very significant as the bond is stretched towards dissociation. Only the $\{1\sigma_g, 1\sigma_u\}$ active space can correctly dissociate into the $\text{H}(1s) \cdots \text{H}(1s)$ ground state of the dissociated fragments (Fig. 2B). In contrast, the binding curves for the $\{1\sigma_g, 2\sigma_g\}$ and $\{1\sigma_g, 2\sigma_u\}$ solutions mirrors the RHF energy as the corresponding wave functions are close to a single Slater determinant at all geometries, with $(1\sigma_g)$ occupations at dissociation of 1.997 and 1.999 respectively. Notably, the stationary points preserve the character of the active orbitals along the po-

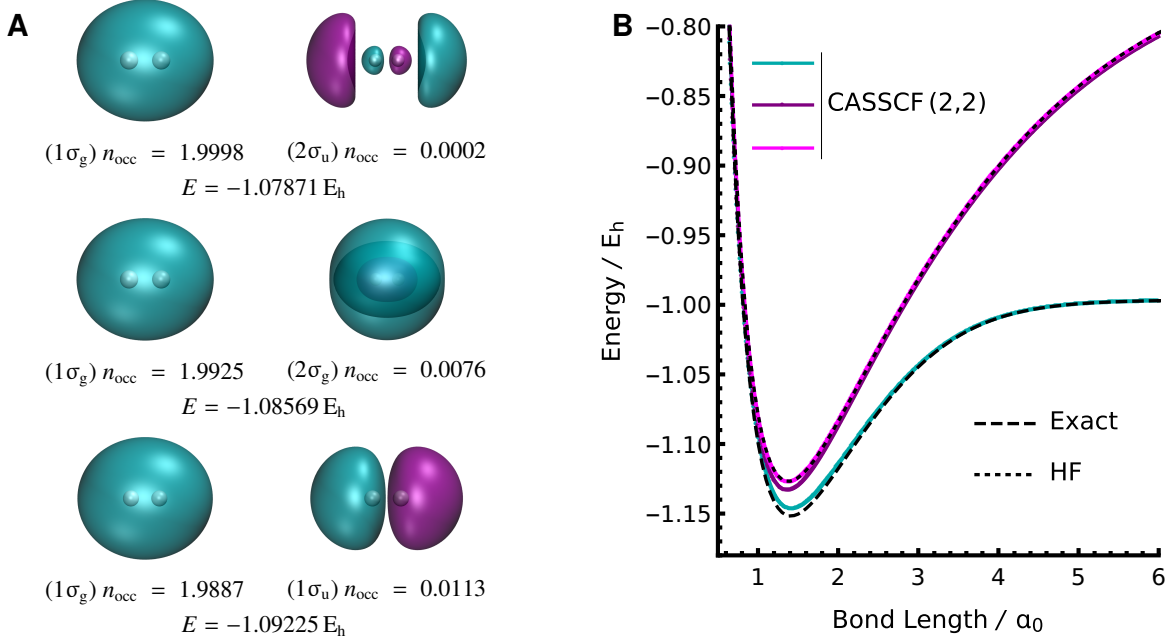


FIG. 2: There are three SS-CASSCF(2,2) solutions that represent the exact ground state in H_2 . **(A)** Comparison of the natural orbitals for each ground-state solution at $R = 1.0 a_0$. **(B)** Only the lowest-energy solution dissociates correctly, while the higher-energy solutions mirror the restricted Hartree–Fock binding curve.

tential energy surface, suggesting that SS-CASSCF solutions exhibit some degree of diabatic character.

The same pattern of solutions is observed for the other closed-shell solutions. However, the $(1\sigma_u)^2$ configuration exhibits an additional multiple solution where the nearly unoccupied active orbital corresponds to a symmetry-broken 2s-like orbital localised on either the left or right H atom, leading to a two-fold degenerate pair of stationary points.

These results indicate that additional solutions can arise from the free choice of virtual orbitals when the active space is larger than required for the degree of static correlation. Malrieu and co-workers elegantly summarised this phenomenon by stating that “*the so-called valence CASSCF wave function does not necessarily keep a valence character when the wave function concentrates on a closed-shell valence bond structure*”.¹¹³ Therefore, we expect that the number of ground state solutions will increase combinatorially with the number of active orbitals or the basis set size, and the number of unphysical solutions can grow for larger active spaces even though the correct ground state solution will become more accurate. Table II demonstrates this increase for H_2 using the 6-311G basis set with three basis functions for each hydrogen atom.¹¹⁴ Taking the (3,2) active space as an example, there are two redundant active orbitals beyond the $1\sigma_g$ that must be chosen from the five remaining orbitals, giving a total of ten solutions through the binomial coefficient $\binom{5}{2} = 10$. The relative energy ordering of these additional solutions will depend on the amount of dynamic correlation captured by the redundant active orbitals, which may not correspond with the same orbital required to capture the static correlation in the dissociation limit. This phenomenon has previously been described for MgO, where oxygen-centred

orbitals are preferred over the magnesium d orbitals,⁹⁰ and transition metal compounds where non-valence d orbitals may be preferred over certain valence d orbitals.¹¹⁵

TABLE II: Close-lying ground-state ($n, 2$) SS-CASSCF energies (E_h) of H_2 at $R = 1 a_0$ using the 6-311G basis set for various active space size n .

SS(1,2): HF	-1.08025				
SS(2,2)	-1.09429	-1.08866	-1.08074	-1.08033	-1.08026
SS(3,2)	-1.10195	-1.09500	-1.09436	-1.09429	-1.08904
	-1.08886	-1.08867	-1.08082	-1.08075	-1.08034
SS(4,2)	-1.10251	-1.10212	-1.10196	-1.09507	-1.09500
	-1.09437	-1.08923	-1.08905	-1.08886	-1.08083
SS(5,2)	-1.10267	-1.10251	-1.10213	-1.09507	-1.08924
SS(6,2): FCI	-1.10267				

3. Open-shell singlet and triplet excitations

The low-lying open-shell triplet and singlet $(1\sigma_g)^1(1\sigma_u)^1$ configurations are represented by only one SS-CASSCF(2,2) solution across the full binding curve (Fig. 1). These single solutions arise because all the active orbitals are required to describe the two-configurational static correlation and there is no flexibility for multiple solutions to exist. In addition, SS-CASSCF(2,2) gives an accurate representation of the open-shell $(1\sigma_{g/u})^1(2\sigma_{g/u})^1$ configurations. However, the accuracy of these solutions deteriorates in the dissociation limit, where additional symmetry broken solutions can be identified (Fig. 3). These additional solutions break spatial symmetry and

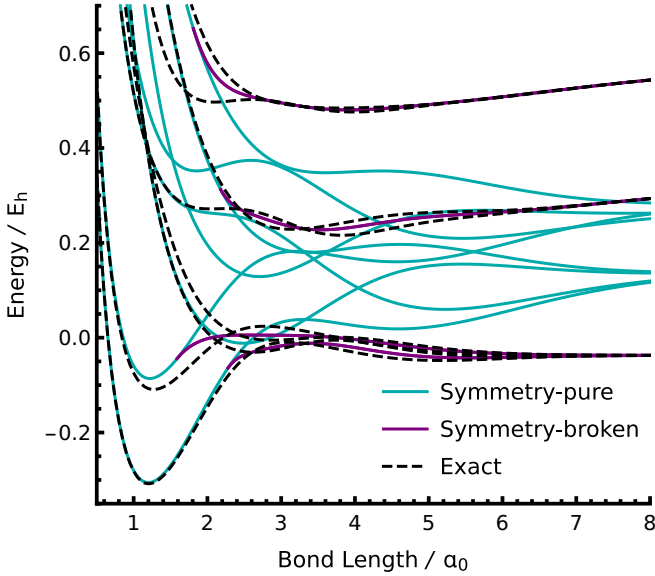


FIG. 3: Spontaneous symmetry breaking occurs when the active space is not large enough to capture all the important configurations in the physical wave function, as illustrated for the 1s 2s states in the dissociation of H₂ (6-31G).

spontaneously appear at instability thresholds that are multi-configurational analogues to the Coulson–Fischer points⁴⁴ in HF theory.^{45,116–119} Each stationary point is a pure singlet or triplet state and has a two-fold degeneracy, reflecting the left-right symmetry of the molecule.

The origin of this symmetry breaking is explained by considering the correlation processes involved in the excited dissociation limit. These excited states dissociate to hydrogenic (1s)¹(2s)¹ configurations, where the occupied 1s and 2s orbitals can either be on the same or different atomic centres. Taking the latter case as an example, the corresponding open-shell singlet wave function at large nuclear separations has the form

$$|\Psi\rangle = \frac{1}{2}(|1s_L 2s_R\rangle + |1s_R 2s_L\rangle)(|\alpha\beta\rangle - |\beta\alpha\rangle). \quad (15)$$

Correctly describing this wave function requires an active space with four spatial orbitals {1s_L, 1s_R, 2s_L, 2s_R}, or equivalently {1σ_g, 1σ_u, 2σ_g, 2σ_u}, and thus the SS-CASSCF(2,2) approximation is insufficient for these correlation mechanisms. Instead, the symmetry breaking reduces the SS-CASSCF(2,2) wave function to a subset of the dominant configurations, e.g.

$$|\tilde{\Psi}\rangle = \frac{1}{\sqrt{2}}|1s_L 2s_R\rangle(|\alpha\beta\rangle - |\beta\alpha\rangle). \quad (16)$$

The CASSCF configurations corresponding to each symmetry-broken solution are assigned in Table III. This “pinning” of the wave function onto particular electronic configurations is directly analogous to the symmetry breaking phenomena observed in HF theory^{120,121} and demonstrates that the active space is too small to fully account for the static correlation.

From the energy landscape perspective, the onset of symmetry-broken CASSCF(2,2) states is associated with a

State	Energy / E _h	$\langle S^2 \rangle$	Configuration
A	0.543355	0.00	$\begin{cases} 1s_L 2s_L\rangle (\alpha\beta\rangle - \beta\alpha\rangle) \\ 1s_R 2s_R\rangle (\alpha\beta\rangle - \beta\alpha\rangle) \end{cases}$
B	0.293363	2.00	$\begin{cases} 1s_L 2s_L\rangle (\alpha\beta\rangle + \beta\alpha\rangle) \\ 1s_R 2s_R\rangle (\alpha\beta\rangle + \beta\alpha\rangle) \end{cases}$
C	-0.037221	0.00	$\begin{cases} 1s_L 2s_R\rangle (\alpha\beta\rangle - \beta\alpha\rangle) \\ 1s_R 2s_L\rangle (\alpha\beta\rangle - \beta\alpha\rangle) \end{cases}$
D	-0.037499	2.00	$\begin{cases} 1s_L 2s_R\rangle (\alpha\beta\rangle + \beta\alpha\rangle) \\ 1s_R 2s_L\rangle (\alpha\beta\rangle + \beta\alpha\rangle) \end{cases}$

TABLE III: The symmetry-broken CASSCF(2,2) solutions in the dissociation of H₂ are two-fold degenerate and represent dominant configurations in the exact excitations.

change in the Hessian index for the associated symmetry-pure solutions. For example, the symmetry-broken state D emerges from the symmetry-pure (1σ_g)¹(2σ_g)¹ triplet state at an instability threshold close to $R = 2.28 a_0$. The Hessian index of the symmetry-pure state changes from 2 to 3 at this point, while the symmetry-broken solutions form index-2 saddle points, leading to a higher-index analogue of a cusp catastrophe.^{42,43,122} Practically, the emergence of a zero Hessian eigenvalue at these instability thresholds may hinder the numerical optimisation of these higher-energy stationary points. It is also interesting to note that, while the symmetry-broken solutions describe two degenerate FCI states at dissociation, they only connect to one of the corresponding symmetry-pure solutions in the equilibrium region. Consequently, one cannot rely on these additional solutions to obtain an accurate and continuous representation of every excited state across all geometries.

B. Conical Intersection in methylene

We next consider the bending mode of methylene, which has a diradical ground state with ³B₁ symmetry and a low-lying 1¹A₁ excited state. The bond length was fixed to the value $R(\text{C-H}) = 2.11 a_0$ identified by Bauschlicher and Taylor^{123,124} and the 6-31G basis set was used.¹¹² Methylene has a long history as a benchmark for electronic structure theory.¹²⁵ One of the primary questions is the description of the conical intersection between the low-lying ³B₁ and 1¹A₁ states.

1. Local minima for the minimal (2,2) active space

A minimal two-configuration wave function is required to qualitatively describe both the lowest-energy singlet S₀ (¹A₁) and diradical triplet T₀ (³B₁) states.¹²³ Therefore, we begin by analysing the SS-CASSCF(2,2) energy landscape. The S₀ and T₀ are the ground state for small and large bond angles, respectively, and provide an example of a conical intersection separating the two regimes. At bond angles of 76°, 102° and 130°, a large number of stationary points can be identified with a variety of Hessian indices. Therefore, we simplify our analysis by focussing on a subset of low-energy solutions that resemble the desired physical states (Fig. 4).

The energetic minimum of the S₀ state occurs at a bond angle of 103.7°. While the S₀ state is the first excited state at this

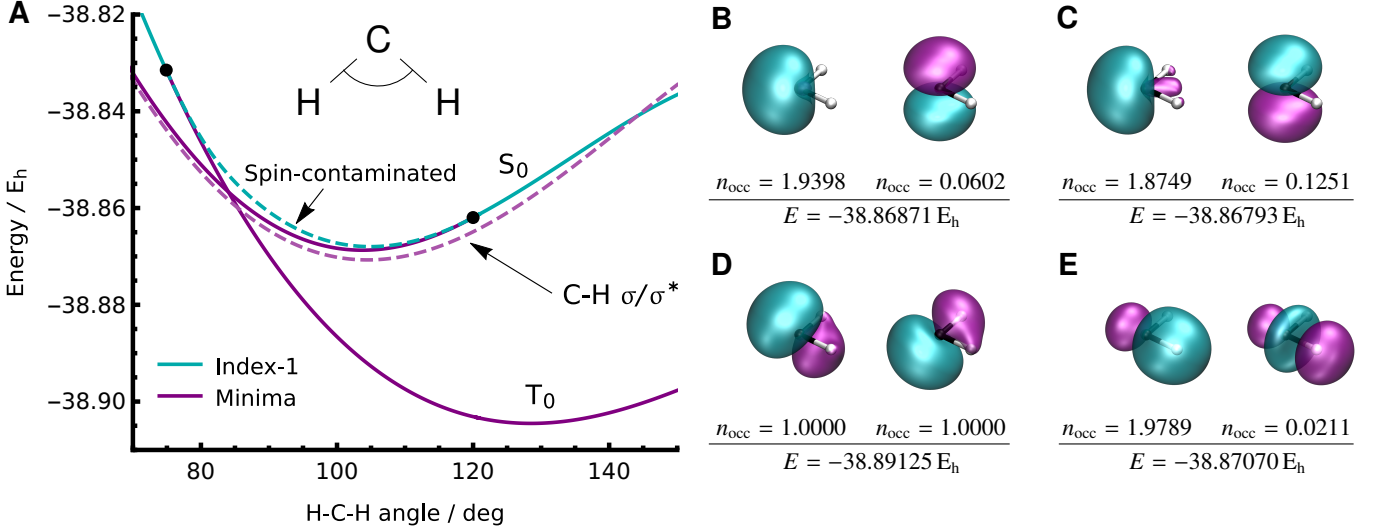


FIG. 4: Low-lying SS-CASSCF(2,2) in the bending mode of methylene represent the 1^3B_1 and 1^1A_1 configurations. **(A)** Both states remain local minima for a short region beyond the conical intersection (solid purple) before becoming an index-1 saddle point (solid cyan). An additional spin-contaminated index-1 saddle point (dashed cyan) connects the two instability thresholds (black dots). Two degenerate local minima exist everywhere along the bending curve (dashed purple) with an active space containing C-H bonding σ and antibonding σ^* orbitals. **(B–E)** The natural orbitals at a bond angle of 103.7° are illustrated for each solution.

geometry, we find that the corresponding SS-CASSCF(2,2) stationary point is a local minimum rather than an index-1 saddle point. This incorrect Hessian index arises from a root flip in the configuration space, where the singlet state is the ground state for the corresponding active orbitals. When the bond angle increases, this singlet state eventually becomes an index-1 saddle point. Similarly, when the bond angle decreases from 103.7° , the T_0 state remains a local minimum beyond the conical intersection where it becomes the first excited state. This process behaves like an unphysical hysteresis, where the ground state remains a local minimum for a small region after a conical intersection before becoming an index-1 saddle point at an instability threshold. An additional index-1 saddle point can be identified that connects these two solutions and coalesces with each local minimum at the two instability thresholds. This unphysical index-1 stationary point is two-fold degenerate, has symmetry-pure spatial orbitals, but is spin contaminated with an $\langle \hat{S}^2 \rangle$ value that changes continuously from 0 to 2 as it connects the singlet and triplet states. Similar patterns of coalescing solutions have been observed in single determinant SCF approximations,^{43,116,126,127} particularly in the generalised HF representation of conical intersections between states with different $\langle \hat{S}_z \rangle$ values.¹²⁸ In contrast to symmetry-broken SCF solutions, the spin contamination observed here arises from the mixture of singlet and triplet states in the configurational part of the CASSCF wave function.

Since the S_0 solution has only one significantly occupied active orbital, we might predict there to be closely-related solutions that have alternative redundant orbitals with $n_{occ} \approx 0$. Indeed, there are a pair of degenerate local minima that lie slightly lower in energy than the S_0 solution. In contrast to the H_2 ground state, including the inactive space means that

methylene has multiple doubly occupied orbitals, and thus the active orbital with $n_{occ} \approx 2$ may also change between different solutions. The active orbitals for these symmetry-broken solutions are localised bonding σ and anti-bonding σ^* orbitals for one of the two C–H bonds, and the degeneracy accounts for the two possible ways to localise onto one bond. Notably, the symmetry breaking here is associated with an active space that is too large, in contrast to H_2 where symmetry breaking arises from an insufficient active space for the static correlation. These solutions are local minima across all the bond angles considered. While they provide an accurate energy for the S_0 state at small bond angles, this deteriorates for large angles as the active space cannot describe the diradical open-shell $^1\Sigma_g^+$ state at the linear geometry. Their existence indicates that the C–H σ/σ^* configurations provide an important contribution to static correlation and should ideally be included in the active space, as suggested by Bauschlicher and Taylor.^{123,124}

2. Full valence active space

Using the full-valence (6,6) active space, we find that the symmetry-pure singlet state is now correctly represented by an index-1 saddle point at a bond angle of 102° (Fig. 5). The unique downhill direction corresponds to a rotation in the configuration space only, as expected for the first excited state. Despite the larger active space, a root flip still occurs as the states approach the singlet-triplet conical intersection at 82.2° , with the singlet state becoming a local minimum at 89.6° and the triplet state becoming an index-1 saddle point at 77.0° . Like the (2,2) active space, a degenerate pair of unphysical, spin-contaminated index-1 saddle points connect the solutions that cross at the conical intersection. This phenomenon occurs because the orbital optimisation can lower the target ex-

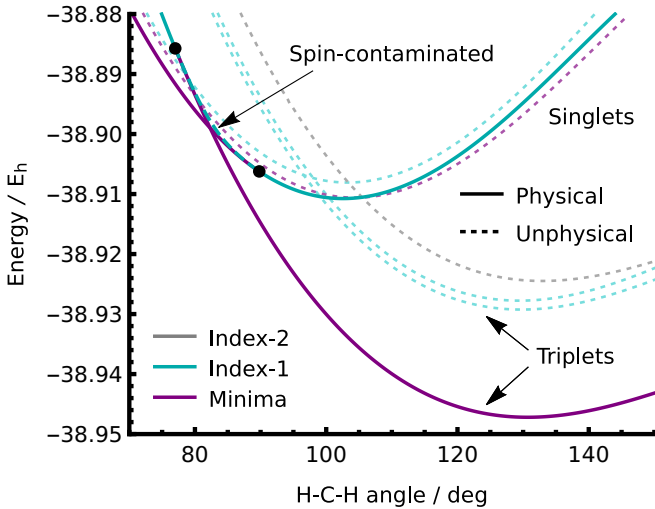


FIG. 5: Low-lying SS-CASSCF(6,6) for the bending mode of methylene represent the 1^3B_1 and 1^1A_1 configurations. The full valence (6,6) active space introduces more unphysical solutions, but does not remove the spin-contaminated solution that arises at the conical intersection.

cited state below the corresponding ground state configuration when the energy gap becomes small. Therefore, while larger active spaces will reduce the range of molecular geometries affected, these unphysical local minima will be common for state-specific conical intersections.

While the larger active space alleviates root flipping, it also causes more unphysical solutions associated with redundant active orbitals. For example, the triplet ground state (dominated by two configurations) is represented by one SS-CASSCF(2,2) solution, but there are several higher-energy solutions in the (6,6) active space. Analogously to the H_2 ground state, these additional solutions have a higher Hessian index, with two index-1 and one index-2 stationary point represented in Fig. 5. Again, the main difference from the true ground state are the active orbitals with occupation numbers close to zero, as illustrated for the global minimum and lowest-energy index-1 saddle point in Fig. 6. Furthermore, we find an additional local minimum and index-1 saddle point that represent the 1^1A_1 state. While all the triplet solutions give approximately the same equilibrium bond angle, the unphysical stationary points shift the conical intersection to coincide with the singlet equilibrium geometry. This qualitative change in the energy surface would create a near-barrierless decay from the singlet excited state to the triplet ground state, demonstrating the importance of verifying the physicality of state-specific solutions.

C. Avoided crossing in Lithium Fluoride

1. Physicality of multiple solutions

The LiF binding curve provides a typical example of an avoided crossing. The ground state has ionic character at equilibrium, but becomes a covalent state with almost no dipole moment in the dissociation limit. Multiple HF solutions are known to behave “quasi-diabolically” and cross each other at the phys-

ical avoided crossing.^{50,129} On the other hand, Bauschlicher and Langhoff demonstrated that this avoided crossing can lead to discontinuities in the CASSCF ground- and excited-state energy surfaces.¹³⁰ Here, we start by considering the state-specific singlet CASSCF solutions in the 6-31G basis set.

Using the minimal (2,2) active, we search for stationary points with Hessian indices of 0 to 10 at $R(\text{Li}-\text{F}) = 2.75 \text{ \AA}$ (near the equilibrium geometry), using 1000 random starting points for each index. The active space for the SS-CASSCF global minimum contains the valence bonding σ and antibonding σ^* orbitals with occupation numbers close to 2 and 0, respectively (Fig. 7B). Because the exact wave function is dominated by a single closed-shell configuration, there are many additional solutions that are close to the ground-state energy at the equilibrium geometry. For example, the second lowest energy solution has an active space containing the out-of-plane fluorine $2p_{x/y}$ and $3p_{x/y}$ orbitals with occupation numbers close to 2 and 0, respectively (Fig. 7C). This active space accounts for the radial correlation on the fluorine atom, providing a more balanced description of F and F^- .¹³⁰ In contrast, the exact excited state is more multiconfigurational at short bond lengths and is accurately represented by only one solution (Fig. 7D), alongside a spurious symmetry-broken solution with diradical character (Fig. 7E). These characteristics are reversed for bond lengths longer than the avoided crossing, where the excited state has closed-shell character with a large number of solutions and the ground state is represented by only two solutions.

State-specific CASSCF solutions can behave both quasi-diabolically and adiabatically in the vicinity of the avoided crossing. As the bond length changes, the unphysical solutions do not have the correct active orbitals to capture the strong correlation at the avoided crossing. Therefore, the two lowest-energy unphysical solutions intersect quasi-diabolically (dark purple in Fig. 7A, corresponding to the solutions in Fig. 7C and 7E). On the other hand, the physically meaningful solutions behave adiabatically and correctly avoid each other (cyan in Fig. 7A). In principle, a linear expansion of both the quasi-diabatic and adiabatic states may provide a more accurate representation of the avoided crossing by introducing some of the dynamic correlation captured by the unphysical solutions. This expansion would require a multiconfigurational variant of nonorthogonal CI, where the Hamiltonian and overlap matrix elements can be efficiently computed using the nonorthogonal framework developed in Refs. 98 and 99.

While a complete description of the avoided crossing requires dynamic correlation,¹³¹ the advantage of state-specific orbital relaxation is still clear in the dissociation limit. The physical SS-CASSCF excited state tends towards the exact FCI energy for the separated $\text{Li}^+ \cdots \text{F}^-$ configuration, while state-averaged calculations with an equal weighting for the two states overestimates the energy of this excited state (Fig. 7A). In this SS-CASSCF solution, the σ and σ^* orbitals (Fig. 7A) both localise to give $2p_z$ orbitals that accurately represent the F^- anion. Consequently, as expected, the state-specific formalism provides a more accurate representation of this charge transfer excitation than a state-averaged approach.

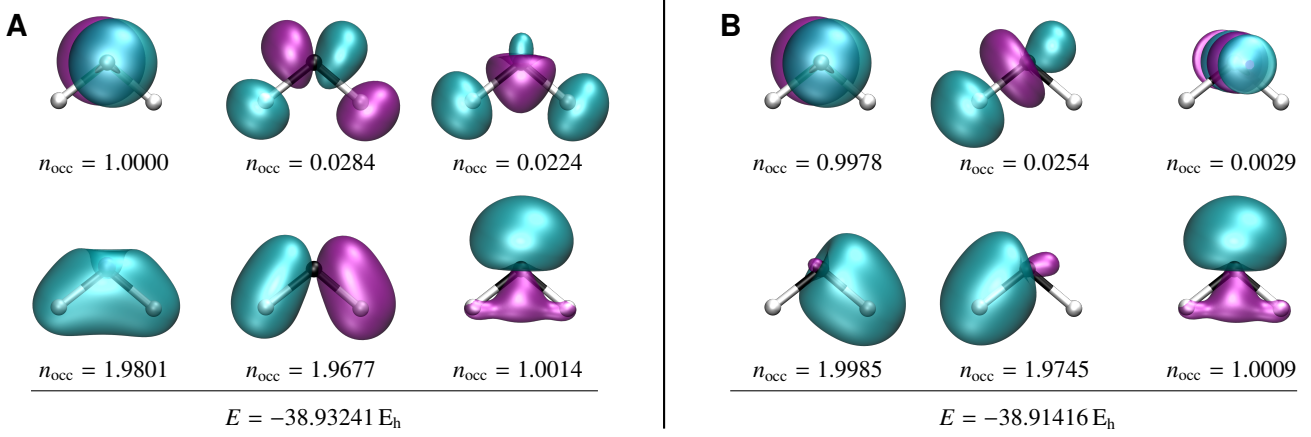


FIG. 6: Comparison of the active orbitals for the two lowest energy triplet CASSCF solutions for CH_2 (6-31G) using the full valence (6,6) active space at a bond angle of 102° . (A) The active orbitals for the local minimum represent the chemically intuitive valence space. (B) For the unphysical index-1 saddle point, one of the antibonding C–H σ^* orbitals with $n_{\text{occ}} \approx 0$ is replaced by a carbon 3p orbital with $n_{\text{occ}} = 0.0029$. The remaining σ and σ^* orbitals localise onto the C–H bonds.

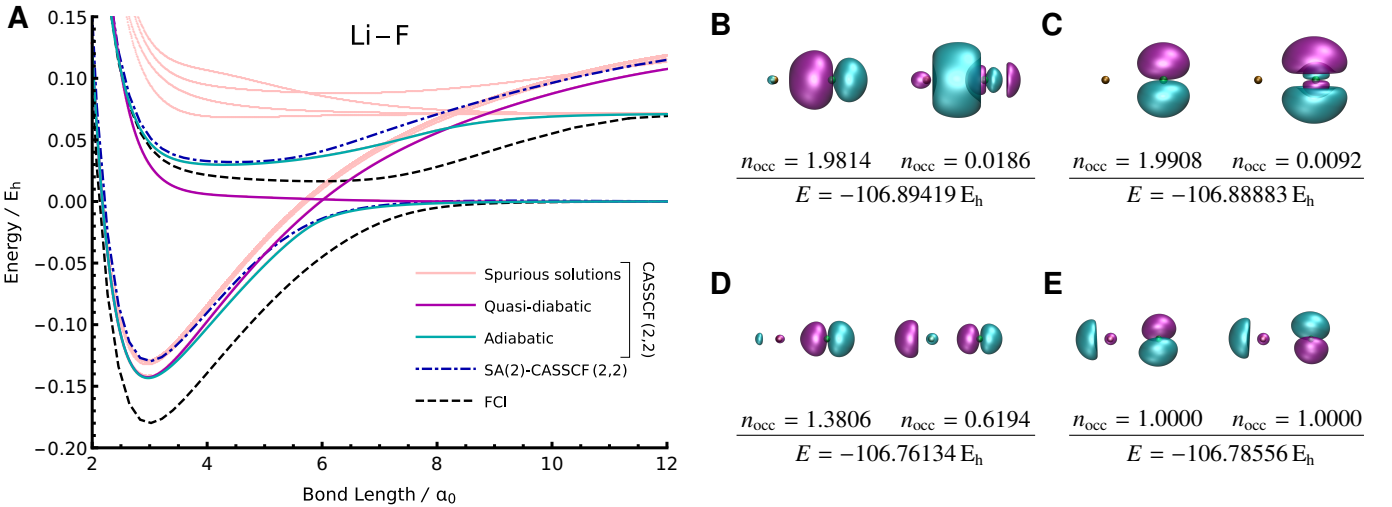


FIG. 7: (A) The SS-CASSCF (2,2) approach gives many solutions for the LiF binding curve (6-31G) when the ground or excited state is dominated by a single configuration. Ground- and excited-state solutions with a suitable active space (B and D) behave adiabatically at the avoided crossing (cyan lines). Additional solutions with unsuitable active orbitals can represent either the ionic equilibrium configuration (C) or the covalent dissociation configuration (E), and behave quasi-diabatically at the avoided crossing (purple lines). The active orbitals are plotted at $R(\text{Li}-\text{F}) = 4 a_0$. Exact FCI and SA(2)-CASSCF (2,2) data are taken from Ref. 50.

2. Elucidating the Bauschlicher–Langhoff discontinuity

The seminal CASSCF investigation of LiF, by Bauschlicher and Langhoff, highlighted the presence of a discontinuity in the ground-state dipole moment in the vicinity of the avoided crossing.¹³⁰ This discontinuity is a signature of a discontinuity in the wave function, which manifests as a cusp in the corresponding energy surface. This phenomenon, which we name the “Bauschlicher–Langhoff discontinuity”, has long been used as key evidence for the potential issues of state-specific calculations in the vicinity of an avoided crossing. Malrieu and co-workers attributed its origin to a near degeneracy between the closed-shell ionic and the open-shell covalent configura-

tions, and described a lower-energy covalent state that emerges from a potential symmetry-breaking point as the bond length increases.¹¹³ The framework developed here, and the advance in computing over the past 30 years, now allows this topological characterisation to be rigorously tested.

To identify the relevant solutions, we searched for minima and index-1 saddle points at a bond length of $8.50 a_0$ using 1000 random starting points, a (2, 2) active space, and the original basis set described in Ref. 130. At $R(\text{Li}-\text{F}) = 8.5 a_0$, the global minimum corresponds to the covalent structure identified in Ref. 113. In addition, two local minima and two index-1 saddle points exist at higher energies, representing the ionic

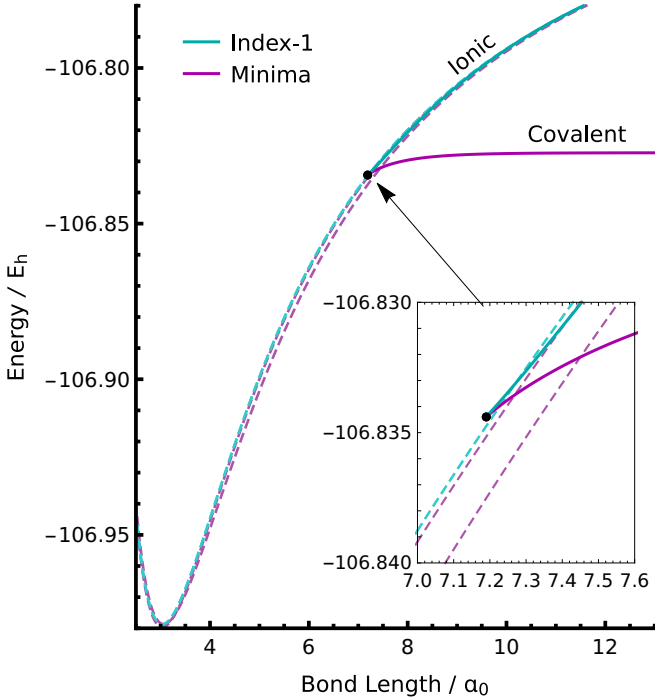


FIG. 8: Topology of the low-energy SS-CASSCF (2, 2) solutions near the Bauschlicher–Langhoff discontinuity in LiF,^{113,130} using the basis set defined in Ref. 130. A cusp in the ground-state energy occurs when two local minima cross, while the covalent structure coalesces with an index-1 saddle point at a pair annihilation point (black dot).

configurations (Fig. 8). As the bond length is shortened, there is a crossing between the lowest energy ionic and covalent minima near $R(\text{Li–F}) = 7.4 \text{ } a_0$, which we believe corresponds to the previously described discontinuity.^{113,130}

Topologically, two non-degenerate minima cannot coalesce without the presence of an index-1 saddle point, and thus the disappearance described by Malrieu and co-workers cannot be the full picture.¹¹³ Instead, we find that the covalent structure crosses the two lowest-energy local minima and eventually coalesces with an index-1 saddle point representing the ionic configurations. Following the downhill directions from this index-1 saddle points reveals that it connects the covalent local minimum with the lowest-energy ionic local minimum. Furthermore, the downhill Hessian eigenvector has significant orbital and CI components, which highlights the strong coupling between the different degrees of freedom in the vicinity of the avoided crossing. Both solutions disappear at this point (black dot in Fig. 8), and thus there is no quasi-diabatic covalent solution at shorter bond lengths.

In the mathematical framework of catastrophe theory,¹³² this type of coalescence can be classified as a fold catastrophe, or a pair annihilation point. This class of singularities have previously been identified and characterised for multiple HF solutions,¹¹⁶ where they most commonly occur in asymmetric molecules, for example LiF,^{50,129} H–Z⁴³ (for a partial nuclear charge Z), and ethylene analogues.⁴³ The discontinuous jump

in the energy at the pair annihilation point in LiF will create issues for calculations that attempt to follow the covalent solution across multiple bond lengths, making these solutions unsuitable for techniques such as *ab initio* molecular dynamics. Furthermore, since the lowest energy covalent and ionic local minima cross rather than coalesce, the gradient at the crossing point is discontinuous and there is an unphysical cusp in the energy.

The absence of this pair annihilation point using 6-31G compared to Bauschlicher and Langhoff’s basis set demonstrates how the topology of multiple CASSCF solutions can be affected by the AO basis. We suspect that these differences arise from the subtle changes in the underlying energy landscape that affect the relative stability of different solutions. However, these results demonstrate the danger of generalising conclusions from one basis set to another, even for the same molecule.

IV. Concluding Remarks

State-specific approximations promise to provide a more balanced representation of electronic excitations by independently optimising both the ground- and excited-state wave functions. In this work, we have investigated the energy landscape for excited state-specific stationary points in the multi-configurational CASSCF approach. We have shown how state-specific approximations can accurately describe high-energy and charge transfer excitations, beyond the reach of state-averaged calculations with small active spaces. However, the CASSCF energy landscape can have a large number of stationary points, which complicates the selection and interpretation of physically relevant solutions.

Multiple stationary points in state-specific CASSCF calculations arise through two primary mechanisms. Firstly, many solutions occur when the active space is too large for the static correlation that must be described. In this case, the redundant active orbitals with $n_{\text{occ}} \approx 0$ can be interchanged with virtual orbitals without significantly changing the energy, creating a series of stationary points with an increasing number of downhill Hessian eigen-directions. Active orbitals with $n_{\text{occ}} \approx 2$ can be interchanged with doubly occupied inactive orbitals in a similar fashion. On the other hand, symmetry broken solutions occur when the active space is too small to describe the static correlation mechanisms, causing the CASSCF wave function to become “pinned” onto a subset of the configurations in the exact wave function. These results demonstrate the importance of finding a “Goldilocks region”, where the active space is neither too large or too small, but just right.

Unphysical solutions can have important consequences for the resulting potential energy surfaces. For example, while choosing the wrong active space only introduces a small error when the wave function is dominated by a single closed-shell configuration, it can prevent the CASSCF wave function from correctly capturing static correlation when the molecular structure changes. The active space for stationary points does not change significantly along a reaction coordinate, meaning that the incorrect active orbitals remain for all geometries. For ground-state calculations, one can rely on following downhill directions away from saddle points to obtain a more suitable local minimum, hopefully with the best active space. However, it is hard to predict which Hessian index will give the most

physical stationary point for an excited state, and thus choosing the most accurate excited-state stationary point is challenging without prior chemical intuition. It has long been known that the right choice of active orbitals is key to the success of CASSCF, but the current results demonstrate the severity of this challenge for state-specific excitations.

In addition, we have investigated the topology of SS-CASSCF(2, 2) solutions near the singlet-triplet conical intersection in CH₂ and the covalent-ionic avoided crossing in LiF. We observe unphysical root flipping where the CH₂ excited state solution is a local minimum near the conical intersection, before becoming an index-1 saddle point further along the reaction trajectory. This phenomenon occurs because the state-specific orbital optimisation artificially stabilises the local minima, and is still present in the full valence (6, 6) active space. Furthermore, the change in Hessian index is associated with an additional spin-contaminated index-1 saddle point that connects the singlet and triplet stationary points. The presence of zero Hessian eigenvalues at these instability thresholds may cause numerical issues for second-order optimisation algorithms. On the other hand, for the LiF avoided crossing, we have observed the coalescence of the local covalent minimum with an index-1 saddle point representing the ionic state, which both disappear entirely at shorter bond lengths. While this pairwise coalescence depends on the basis set, it would catastrophically affect the applicability of SS-CASSCF for generating continuous potential energy surfaces.

Moving forwards, SS-CASSCF calculations must overcome the troublesome issues of multiple solutions. Practical solutions may rely on the identification of suitable initial guesses from more black-box techniques, or by focussing on optimisation algorithms that target desirable excited-state physical properties (e.g. dipole moments), such as the generalized variational principles developed by Hanscam and Neuscammman.⁹⁰ Alternatively, more bespoke excited-state wave function *ansätze*, such as minimal configuration state functions⁷² or excited-state mean-field theory,^{67,68,71} may remove unphysical solutions associated with redundant active orbitals and avoid the disappearance of solutions at pairwise coalescence points. Surmounting these issues will allow the benefits of state-specific calculations for computing excited states with bespoke orbitals and small active spaces to be fully realised.

Acknowledgements

H.G.A.B was supported by New College, Oxford, through the Astor Junior Research Fellowship. The authors thank David Tew for support and computing resources.

References

- ¹Burton, H. G. A. Energy Landscape of State-Specific Electronic Structure Theory. *J. Chem. Theory Comput.* **2022**, *18*, 1512.
- ²Olsen, J.; Jørgensen, P.; Yeager, D. L. Multiconfigurational Hartree–Fock studies of avoided curve crossing using the Newton–Raphson technique. *J. Chem. Phys.* **1982**, *76*, 527.
- ³Golab, J. T.; Yeager, D. L.; Jørgensen, P. Proper characterization of MC SCF stationary points. *Chem. Phys.* **1983**, *78*, 175.
- ⁴Olsen, J.; Yeager, D. L.; Jørgensen, P. Optimization and Characterization of a Multiconfigurational Self-Consistent Field (MCSCF) State. In *Adv. Chem. Phys.*; John Wiley and Sons, Ltd, 1983; pp 1–176.
- ⁵Golab, J. T.; Yeager, D. L.; Jørgensen, P. Multiple stationary point representations in MC SCF calculations. *Chem. Phys.* **1985**, *93*, 83.
- ⁶Bacalí, N. C.; Xiong, Z.; Zang, J.; Karaoulanis, D. Computing correct truncated excited state wavefunctions. *AIP Conf. Proc.* **2016**, *1790*, 020007.
- ⁷Bacalí, N. C. If Truncated Wave Functions of Excited State Energy Saddle Points Are Computed as Energy Minima, Where Is the Saddle Point? In *Theoretical Chemistry for Advanced Nanomaterials: Functional Analysis by Computation and Experiment*; Onishi, T., Ed.; Springer Singapore: Singapore, 2020; p 465.
- ⁸Runge, E.; Gross, E. K. U. Density-Functional Theory for Time-Dependent Systems. *Phys. Rev. Lett.* **1984**, *52*, 997.
- ⁹Drew, A.; Head-Gordon, M. Single-Reference ab Initio Methods for the Calculation of Excited States of Large Molecules. *Chem. Rev.* **2005**, *105*, 4009.
- ¹⁰Burke, K.; Werschnik, J.; Gross, E. K. U. Time-dependent density functional theory: Past, present, and future. *J. Chem. Phys.* **2005**, *123*, 062206.
- ¹¹Hait, D.; Rettig, A.; Head-Gordon, M. Beyond the Coulson–Fischer point: characterizing single excitation CI and TDDFT for excited states in single bond dissociations. *Phys. Chem. Chem. Phys.* **2019**, *21*, 21761.
- ¹²Maitra, N. T.; Zhang, F.; Cave, R. J.; Burke, K. Double excitations within time-dependent density functional theory linear response. *J. Chem. Phys.* **2004**, *120*, 5932.
- ¹³Schirmer, J. Beyond the random-phase approximation: A new approximation scheme for the polarization propagator. *Phys. Rev. A* **1982**, *26*, 2395.
- ¹⁴Drew, A.; Wormit, M. The algebraic diagrammatic construction scheme for the polarization propagator for the calculation of excited states. *WIREs Comput. Mol. Sci.* **2015**, *5*, 82.
- ¹⁵Stanton, J. F.; Bartlett, R. J. The equation of motion coupled-cluster method. A systematic biorthogonal approach to molecular excitation energies, transition probabilities, and excited state properties. *J. Chem. Phys.* **1993**, *98*, 7029.
- ¹⁶Krylov, A. I. Equation-of-Motion Coupled-Cluster Methods for Open-Shell and Electronically Excited Species: The Hitchhiker’s Guide to Fock Space. *Annu. Rev. Phys. Chem.* **2008**, *59*, 433.
- ¹⁷Tozer, D. J. Relationship between Long-Range Charge-Transfer Excitation Energy Error and Integer Discontinuity in Kohn–Sham Theory. *J. Chem. Phys.* **2003**, *119*, 12697.
- ¹⁸Drew, A.; Head-Gordon, M. Failure of Time-Dependent Density Functional Theory for Long-Range Charge-Transfer Excited States: The Zincbacteriochlorin–Bacteriochlorin and Bacteriochlorophyll–Spheroïdene Complexes. *J. Am. Chem. Soc.* **2004**, *126*, 4007.
- ¹⁹McLachlan, A. D.; Ball, M. A. Time-Dependent Hartree–Fock Theory for Molecules. *Rev. Mod. Phys.* **1964**, *36*, 844–855.
- ²⁰Runge, E.; Gross, E. K. U. Density-Functional Theory for Time-Dependent Systems. *Phys. Rev. Lett.* **1984**, *52*, 997–1000.
- ²¹Drew, A.; Head-Gordon, M. Single-Reference Ab Initio Methods for the Calculation of Excited States of Large Molecules. *Chem. Rev.* **2005**, *105*, 4009–4037.
- ²²Burke, K.; Werschnik, J.; Gross, E. K. U. Time-Dependent Density Functional Theory: Past, Present, and Future. *J. Chem. Phys.* **2005**, *123*, 062206.
- ²³Bartlett, R. J. Coupled-Cluster Theory and Its Equation-of-Motion Extensions. *WIREs Comput. Mol. Sci.* **2012**, *2*, 126–138.
- ²⁴Heimlich-Paris, B. Benchmarks for Electronically Excited States with CASSCF Methods. *J. Chem. Theory Comput.* **2019**, *15*, 4170–4179.
- ²⁵Gilbert, A. T. B.; Besley, N. A.; Gill, P. M. W. Self-Consistent Field Calculations of Excited States Using the Maximum Overlap Method (MOM). *J. Phys. Chem. A* **2008**, *112*, 13164.
- ²⁶Barca, G. M. J.; Gilbert, A. T. B.; Gill, P. M. W. Communication: Hartree–Fock description of excited states of H₂. *J. Chem. Phys.* **2014**, *141*, 111104.
- ²⁷Barca, G. M. J.; Gilbert, A. T. B.; Gill, P. M. W. Simple Models for Difficult Electronic Excitations. *J. Chem. Theory Comput.* **2018**, *14*, 1501.
- ²⁸Hait, D.; Head-Gordon, M. Orbital Optimized Density Functional Theory for Electronic Excited States. *J. Phys. Chem. Lett.* **2021**, *12*, 4517.
- ²⁹Hait, D.; Head-Gordon, M. Excited State Orbital Optimization via Minimizing the Square of the Gradient: General Approach and Application to Singly and Doubly Excited States via Density Functional Theory. *J. Chem. Theory Comput.* **2020**, *16*, 1699.
- ³⁰Carter-Fenk, K.; Herbert, J. M. State-Targeted Energy Projection: A Simple and Robust Approach to Orbital Relaxation of Non-Aufbau Self-Consistent Field Solutions. *J. Chem. Theory Comput.* **2020**, *16*, 5067.

- ³¹Levi, G.; Ivanov, A. V.; Jónsson, H. Variational Density Functional Calculations of Excited States via Direct Optimization. *J. Chem. Theory Comput.* **2020**, *16*, 6968.
- ³²Levi, G.; Ivanov, A. V.; Jónsson, H. Variational calculations of excited states via direct optimization of the orbitals in DFT. *Faraday Discuss.* **2020**, *224*, 448.
- ³³Ivanov, A. V.; Gianluca Levi, E. O. J.; Jónsson, H. Method for Calculating Excited Electronic States Using Density Functionals and Direct Orbital Optimization with Real Space Grid or Plane-Wave Basis Set. *J. Chem. Theory Comput.* **2021**, *17*, 5034.
- ³⁴Shea, J. A. R.; Neuscamman, E. Size Consistent Excited States via Algorithmic Transformations between Variational Principles. *J. Chem. Theory Comput.* **2017**, *13*, 6078.
- ³⁵Jankowski, K.; Kowalski, K.; Jankowski, P. Applicability of single-reference coupled-cluster methods to excited states. A model study. *Chem. Phys. Lett.* **1994**, *222*, 608.
- ³⁶Jankowski, K.; Kowalski, K.; Jankowski, P. Multiple Solutions of the Single-Reference Coupled-Cluster Equations. II. Alternative Reference States. *Int. J. Quantum Chem.* **1994**, *53*, 501.
- ³⁷Piecuch, P.; Kowalski, K. In *Computational Chemistry: Reviews of Current Trends*; Leszczynski, J., Ed.; World Scientific, 2000; Vol. 5; Chapter 1. In Search of the Relationship between Multiple Solutions Characterizing Coupled-Cluster Theories, p 1.
- ³⁸Mayhall, N. J.; Raghavachari, K. Multiple Solutions to the Single-Reference CCSD Equations for NiH. *J. Chem. Theory Comput.* **2010**, *6*, 2714.
- ³⁹Lee, J.; Head-Gordon, M. Distinguishing artificial and essential symmetry breaking in a single determinant: approach and application to the C₆₀, C₃₆, and C₂₀ fullerenes. *Phys. Chem. Chem. Phys.* **2019**, *21*, 4763.
- ⁴⁰Kossoски, F.; Marie, A.; Scemama, A.; Caffarel, M.; Loos, P.-F. Excited States from State-Specific Orbital-Optimized Pair Coupled Cluster. *J. Chem. Theory Comput.* **2021**, *17*, 4756.
- ⁴¹Marie, A.; Kossoски, F.; Loos, P.-F. Variational coupled cluster for ground and excited states. *J. Chem. Phys.* **2021**, *155*, 104105.
- ⁴²Burton, H. G. A.; Wales, D. J. Energy Landscapes for Electronic Structure. *J. Chem. Theory Comput.* **2021**, *17*, 151.
- ⁴³Burton, H. G. A.; Gross, M.; Thom, A. J. W. Holomorphic Hartree–Fock Theory: The Nature of Two-Electron Problems. *J. Chem. Theory Comput.* **2018**, *14*, 607.
- ⁴⁴Coulson, C. A.; Fischer, I. XXXIV. Notes on the molecular orbital treatment of the hydrogen molecule. *Philos. Mag.* **1949**, *40*, 386.
- ⁴⁵Fukutome, H. The Unrestricted Hartree–Fock Theory of Chemical Reactions. III: Instability Conditions for Paramagnetic and Spin Density Wave States and Application to Internal Rotation of Ethylene. *Prog. Theor. Phys.* **1973**, *50*, 1433.
- ⁴⁶Fukutome, H. Theory of the Unrestricted Hartree–Fock Equation and Its Solutions. III: Classification of Instabilities and Interconnection Relation between the Eight Classes of UHF Solutions. *Prog. Theor. Phys.* **1974**, *52*, 1766.
- ⁴⁷Fukutome, H. Theory of the Unrestricted Hartree–Fock Equation and Its Solutions III: Classification and Characterization of UHF Solutions by Their Behaviour for Spin Rotation and Time Reversal. *Prog. Theor. Phys.* **1974**, *52*, 115.
- ⁴⁸Ye, H.-Z.; Welborn, M.; Ricke, N. D.; Van Voorhis, T. σ -SCF: A direct energy-targeting method to mean-field excited states. *J. Chem. Phys.* **2017**, *147*, 214104.
- ⁴⁹Thom, A. J. W.; Head-Gordon, M. Locating Multiple Self-Consistent Field Solutions: An Approach Inspired by Metadynamics. *Phys. Rev. Lett.* **2008**, *101*, 193001.
- ⁵⁰Burton, H. G. A.; Thom, A. J. W. Reaching Full Correlation through Nonorthogonal Configuration Interaction: A Second-Order Perturbative Approach. *J. Chem. Theory Comput.* **2020**, *16*, 5586.
- ⁵¹Jensen, K. T.; Benson, R. L.; Cardamone, S.; Thom, A. J. W. Modeling Electron Transfers Using Quasidiabatic Hartree–Fock States. *J. Chem. Theory Comput.* **2018**, *14*, 4629.
- ⁵²Vaucher, A. C.; Reiher, M. Steering Orbital Optimization out of Local Minima and Saddle Points Toward Lower Energy. *J. Chem. Theory Comput.* **2017**, *13*, 1219.
- ⁵³Dong, X.; Mahler, A. D.; Kempfer-Robertson, E. M.; Thompson, L. M. Global Elucidation of Self-Consistent Field Solution Space Using Basin Hopping. *J. Chem. Theory Comput.* **2020**, *16*, 5635.
- ⁵⁴Szabo, A.; Ostlund, N. S. *Modern Quantum Chemistry*; Dover Publications Inc., 1989.
- ⁵⁵Das, G.; Wahl, A. C. Extended Hartree–Fock Wavefunctions: Optimized Valence Configurations for H₂ and Li₂, Optimized Double Configurations for F₂. *J. Chem. Phys.* **1966**, *44*, 87.
- ⁵⁶Roos, B. O.; Taylor, P. R.; Siegbahn, P. E. M. A complete active space SCF method (CASSCF) using a density matrix formulated super-CI. *Chem. Phys.* **1980**, *48*, 157.
- ⁵⁷Roos, B. O. The Complete Active Space SCF method in a Fock-Matrix-Based Super-CI Formulation. *Int. J. Quantum Chem.* **1980**, *18*, 175.
- ⁵⁸Roos, B. O.; Lindh, R.; Malmqvist, P. Å.; Veryazov, V.; Windmark, P.-O. *Multiconfigurational Quantum Chemistry*; Wiley, 2016.
- ⁵⁹Das, G. Multiconfiguration self-consistent field (MCSCF) theory for excited states. *J. Chem. Phys.* **1973**, *58*, 5104.
- ⁶⁰Krauss, M.; Neumann, D. B. The $^5\Sigma_g^+$ states of N₂. *Mol. Phys.* **1976**, *32*, 101.
- ⁶¹Bauschlicher Jr., C. W.; Yarkony, D. R. Electronic structure of CaO. *I. J. Chem. Phys.* **1978**, *68*, 3990.
- ⁶²Bauschlicher Jr., C. W.; Yarkony, D. R. MCSCF wave functions for excited states of polar molecules: Application to BeO. *J. Chem. Phys.* **1980**, *72*, 1138.
- ⁶³Bauschlicher Jr., C. W.; Lengsfeld III, B. H.; Yarkony, D. R. On the low lying singlet states of BeO. *J. Chem. Phys.* **1980**, *73*, 5702.
- ⁶⁴Bauschlicher Jr., C. W.; Silver, D. M.; Yarkony, D. R. An SCF and MCSCF description of the low-lying states of MgO. *J. Chem. Phys.* **1980**, *73*, 2867.
- ⁶⁵Guilher, N.; Malrieu, J.-P.; Maynau, D.; Handrick, K. Unexpected CASSCF Bistability Phenomenon. *Int. J. Quantum Chem.* **1997**, *61*, 45.
- ⁶⁶Angeli, C.; Calzado, C. J.; Cimiraglia, R.; Evangelista, S.; Mayna, D. Multiple complete active space self-consistent field solutions. *Mol. Phys.* **2003**, *101*, 1937.
- ⁶⁷Shea, J. A. R.; Neuscamman, E. A mean field platform for excited state quantum chemistry. *J. Chem. Phys.* **2018**, *149*, 081101.
- ⁶⁸Shea, J. A. R.; Gwin, E.; Neuscamman, E. A Generalized Variational Principle with Applications to Excited State Mean Field Theory. *J. Chem. Theory Comput.* **2020**, *16*, 1526.
- ⁶⁹Zhao, L.; Neuscamman, E. Excited state mean-field theory without automatic differentiation. *J. Chem. Phys.* **2020**, *152*, 204112.
- ⁷⁰Zhao, L.; Neuscamman, E. Density Functional Extension to Excited-State Mean-Field Theory. *J. Chem. Theory Comput.* **2020**, *16*, 164.
- ⁷¹Hardikar, T. S.; Neuscamman, E. A self-consistent field formulation of excited state mean field theory. *J. Chem. Phys.* **2020**, *153*, 164108.
- ⁷²Kossoски, F.; Loos, P.-F. “State-Specific Configuration Interaction for Excited States” **2022**,
- ⁷³Dalgard, E.; Jørgensen, P. Optimization of orbitals for multiconfigurational reference states. *J. Chem. Phys.* **1978**, *69*, 3833.
- ⁷⁴Dalgard, E. A quadratically convergent reference state optimization procedure. *Chem. Phys. Lett.* **1979**, *65*, 559.
- ⁷⁵Yeager, D. L.; Jørgensen, P. Convergency studies of second and approximate second order multiconfigurational Hartree–Fock procedures. *J. Chem. Phys.* **1979**, *71*, 755.
- ⁷⁶Lengsfeld III, B. H. General second order MCSCF theory: A density matrix directed algorithm. *J. Chem. Phys.* **1980**, *73*, 382.
- ⁷⁷Siegbahn, P. E. M.; Almlöf, J.; Heiberg, A.; Roos, B. O. The complete active space SCF (CASSCF) method in a Newton-Raphson formulation with application to the HNO molecule. *J. Chem. Phys.* **1981**, *74*, 2384.
- ⁷⁸Werner, H.-J.; Meyer, W. A quadratically convergent MCSCF method for the simultaneous optimization of several states simultaneous optimization of several states. *J. Chem. Phys.* **1981**, *74*, 5794.
- ⁷⁹Werner, H.-J.; Knowles, P. J. A second order multiconfigurational SCF procedure with optimum convergence. *J. Chem. Phys.* **1985**, *82*, 5053.
- ⁸⁰Yeager, D. L.; Jørgensen, P. A numerical study of the convergency of second and approximate second-order multiconfiguration Hartree–Fock procedures. *Mol. Phys.* **1980**, *39*, 587.
- ⁸¹Yeager, D. L.; Albertsen, P.; Jørgensen, P. Mode damping in multiconfigurational Hartree–Fock procedures. *J. Chem. Phys.* **1980**, *73*, 2811.
- ⁸²Jørgensen, P.; Olsen, J.; Yeager, D. L. Generalizations of Newton–Raphson and multiplicity independent Newton–Raphson approaches in multiconfigurational Hartree–Fock theory. *J. Chem. Phys.* **1981**, *75*, 5802.
- ⁸³Yeager, D. L.; Lynch, D.; Nichols, J.; Jørgensen, P.; Olsen, J. Newton–Raphson Approaches and Generalizations in Multiconfigurational Self-Consistent Field Calculations. *J. Phys. Chem.* **1982**, *86*, 2140.

- ⁸⁴Sun, Q.; Yang, J.; Chan, G. K.-L. A General Second Order Complete Active Space Self-Consistent-Field Solver for Large-Scale Systems. *Chem. Phys. Lett.* **2017**, *683*, 291.
- ⁸⁵Kreplin, D. A.; Knowles, P. J.; Werner, H.-J. Second-order MCSCF optimization revisited. I. Improved algorithms for fast and robust second-order CASSCF convergence. *J. Chem. Phys.* **2019**, *150*, 194106.
- ⁸⁶Kreplin, D. A.; Knowles, P. J.; Werner, H.-J. MCSCF optimization revisited. II. Combined first- and second-order orbital optimization for large molecules. *J. Chem. Phys.* **2020**, *152*, 074102.
- ⁸⁷Rizzo, A.; Yeager, D. L. Characteristics and some peculiarities of multi-configurational self-consistent field stationary points of the Li⁻ ground state. *J. Chem. Phys.* **1990**, *93*, 8011.
- ⁸⁸Zaitsevskii, A.; Malrieu, J.-P. The discontinuities of state-average MCSCF potential surfaces. *Chem. Phys. Lett.* **1994**, *228*, 458.
- ⁸⁹Tran, L. N.; Neuscamman, E. Improving Excited-State Potential Energy Surfaces via Optimal Orbital Shapes. *J. Phys. Chem. A* **2020**, *124*, 8273.
- ⁹⁰Hanscam, R.; Neuscamman, E. Applying Generalized Variational Principles to Excited-State-Specific Complete Active Space Self-consistent Field Theory. *J. Chem. Theory Comput.* **2022**, *18*, 6608.
- ⁹¹Tran, L. N.; Shea, J. A. R.; Neuscamman, E. Tracking Excited States in Wave Function Optimization Using Density Matrices and Variational Principles. *J. Chem. Theory Comput.* **2019**, *15*, 4790.
- ⁹²Helgaker, T.; Jørgensen, P.; Olsen, J. *Molecular Electronic-Structure Theory*; John Wiley & Sons, 2000.
- ⁹³Head-Gordon, M.; Maslen, P. E.; White, C. A. A tensor formulation of many-electron theory in a nonorthogonal single-particle basis. *J. Chem. Phys.* **1998**, *108*, 616.
- ⁹⁴Hylleraas, E. A.; Undheim, B. Numerische Berechnung der 2S-Terme von Ortho- und Par-Helium. *Z. Phys.* **1930**, *65*, 759.
- ⁹⁵MacDonald, J. K. L. Successive Approximations by the Rayleigh-Ritz Variation Method. *Phys. Rev.* **1933**, *43*, 830.
- ⁹⁶Douady, J.; Ellinger, Y.; Subra, R.; Levy, B. Exponential transformation of molecular orbitals: A quadratically convergent SCF procedure. I. General formulation and application to closed-shell ground states. *J. Chem. Phys.* **1980**, *72*, 1452.
- ⁹⁷Van Voorhis, T.; Head-Gordon, M. A geometric approach to direct minimization. *Mol. Phys.* **2002**, *100*, 1713.
- ⁹⁸Burton, H. G. A. Generalized nonorthogonal matrix elements: Unifying Wick's theorem and the Slater-Condon rules. *J. Chem. Phys.* **2021**, *154*, 144109.
- ⁹⁹Burton, H. G. A. Generalized nonorthogonal matrix elements. II: Extension to arbitrary excitations. *J. Chem. Phys.* **2022**, *157*, 204109.
- ¹⁰⁰Mayer, I. *Simple Theorems, Proofs, and Derivations in Quantum Chemistry*; Springer, 2003.
- ¹⁰¹Manni, G. L.; Gunther, K.; Ma, D.; Dobrutz, W. Foundation of Multi-Configurational Quantum Chemistry. In *Quantum Chemistry and Dynamics of Excited States: Methods and Applications*; González, L., Lindh, R., Eds.; John Wiley & Sons, Ltd, 2021; p 133.
- ¹⁰²Löwdin, P.-O. Quantum Theory of Many-Particle Systems. I. Physical Interpretations by Means of Density Matrices, Natural Spin-Orbitals, and Convergence Problems in the Method of Configurational Interaction. *Phys. Rev.* **1955**, *97*, 1474.
- ¹⁰³Docken, K. K.; Hinze, J. LiH Potential Curves and Wavefunctions for X^{1Σ⁺, A^{1Σ⁺, B^{1Π}, ^{3Σ⁺, and ^{3Π}. *J. Chem. Phys.* **1972**, *57*, 4928.}}}
- ¹⁰⁴Cerjan, C. J.; Miller, W. H. On finding transition states. *J. Chem. Phys.* **1981**, *75*, 2800.
- ¹⁰⁵Wales, D. J. Structural and Topological Consequences of Anisotropic Interactions in Clusters. *Faraday Discuss.* **1990**, *86*, 3505.
- ¹⁰⁶Wales, D. J. *Energy Landscapes: Applications to Clusters, Biomolecules and Glasses*; Cambridge University Press: Cambridge, 2004.
- ¹⁰⁷Hoffmann, M. R.; Sherrill, C. D.; Leininger, M. L.; Schaefer III, H. F. Optimization of MCSCF excited states using directions of negative curvature. *Chem. Phys. Lett.* **2002**, *355*, 183.
- ¹⁰⁸Nocedal, J.; Wright, S. *Numerical Optimization*; Springer-Verlag, 2006.
- ¹⁰⁹Sun, Q. et al. Recent developments in the PySCF program package. *J. Chem. Phys.* **2020**, *153*, 024109.
- ¹¹⁰Humphrey, W.; Dalke, A.; Schulten, K. VMD – Visual Molecular Dynamics. *J. Mol. Graph.* **1996**, *14*, 33.
- ¹¹¹Wolfram Research, Inc., Mathematica, Version 12.1. Champaign, Illinois, 2020.
- ¹¹²Ditchfield, R.; Hehre, W. J.; Pople, J. A. Self-Consistent Molecular-Orbital Methods. IX. An Extended Gaussian-Type Basis for Molecular-Orbital Studies of Organic Molecules. *J. Chem. Phys.* **1971**, *54*, 724.
- ¹¹³Sanchez de Meras, A.; Lepetit, M.-B.; Malrieu, J.-P. Discontinuity of valence CASSCF wave functions around weakly avoided crossing between valence configurations. *Chem. Phys. Lett.* **1990**, *172*, 163.
- ¹¹⁴Krishnan, R.; Binkley, J. S.; Seeger, R.; Pople, J. A. Self-consistent Molecular Orbital Methods. XX. A Basis Set for Correlated Wave Functions. *J. Chem. Phys.* **1980**, *72*, 650.
- ¹¹⁵Andersson, K.; Roos, B. O. Excitation energies in the nickel atom studied with the complete active space SCF method and second-order perturbation theory. *Chem. Phys. Lett.* **1992**, *191*, 507.
- ¹¹⁶Fukutome, H. Theory of the Unrestricted Hartree–Fock Equation and Its Solutions. IV: Behavior of UHF Solutions in the Vicinity of Interconnecting Instability Threshold. *Prog. Theor. Phys.* **1975**, *53*, 1320.
- ¹¹⁷Mestechkin, M. M. Restricted Hartree–Fock Method Instability. *Int. J. Quantum Chem.* **1978**, *13*, 469.
- ¹¹⁸Mestechkin, M. Instability Threshold and Peculiar Solutions of Hartree–Fock Equations. *Int. J. Quantum Chem.* **1979**, *15*, 601.
- ¹¹⁹Mestechkin, M. Potential Energy Surface near the Hartree–Fock Instability Threshold. *J. Mol. Struct.: THEOCHEM* **1988**, *181*, 231.
- ¹²⁰Trail, J. R.; Towler, M. D.; Needs, R. J. Unrestricted Hartree–Fock theory of Wigner crystals. *Phys. Rev. B* **2003**, *68*, 045107.
- ¹²¹Burton, H. G. A. Hartree–Fock critical nuclear charge in two-electron atoms. *J. Chem. Phys.* **2021**, *154*, 111103.
- ¹²²Gilmore, R. *Catastrophe Theory for Scientists and Engineers*, 1st ed.; Dover Publications Inc., 1993.
- ¹²³Bauschlicher Jr., C. W.; Taylor, P. R. Benchmark full configuration-interaction calculations on H₂O, F, and F⁻. *J. Chem. Phys.* **1986**, *85*, 2779.
- ¹²⁴Bauschlicher Jr., C. W.; Taylor, P. R. A full CI treatment of the ¹A₁–³B₁ separation in methylene. *J. Chem. Phys.* **1986**, *85*, 6510.
- ¹²⁵Schaefer, H. F. Methylen: A Paradigm for Computational Quantum Chemistry. *Science* **1986**, *231*, 1100.
- ¹²⁶Zaratiadis, R. A.; Burton, H. G. A.; Thom, A. J. W. Towards a Holomorphic Density Functional Theory. *J. Chem. Theory Comput.* **2020**, *16*, 7400.
- ¹²⁷Huyhn, B. C.; Thom, A. J. W. Symmetry in Multiple Self-Consistent-Field Solutions of Transition-Metal Complexes. *J. Chem. Theory Comput.* **2020**, *16*, 904.
- ¹²⁸Jiménez-Hoyos, C. A.; Henderson, T. M.; Scuseria, G. E. Generalized Hartree–Fock Description of Molecular Dissociation. *J. Chem. Theory Comput.* **2011**, *7*, 2667.
- ¹²⁹Thom, A. J. W.; Head-Gordon, M. Hartree–Fock solutions as a quasidiabatic basis for nonorthogonal configuration interaction. *J. Chem. Phys.* **2009**, *131*, 124113.
- ¹³⁰Bauschlicher, C. W.; Langhoff, S. R. Full configuration-interaction study of the ionic-neutral curve crossing in LiF. *J. Chem. Phys.* **1988**, *89*, 4246.
- ¹³¹Malrieu, J.-P.; Heully, J.-L.; Zaitsevskii, A. Multiconfigurational second-order perturbative methods: Overview and comparison of basic properties. *Theor. Chim. Acta* **1995**, *90*, 167.
- ¹³²Thom, R. *Structural Stability and Morphogenesis*, 1st ed.; Westview Press, 1994.

Supporting Information

A. Deriving the CASSCF gradient and second-derivatives

1. Notation and reduced density matrices

Here, we provide explicit expressions for the gradient and Hessian of the CASSCF energy, which are required for quasi-Newton optimisation algorithms. These expressions are derived in detail in Refs. 4 and 92, but we include this pedagogical discussion for completeness. In what follows, the indices m, n, p, q, r, s correspond to arbitrary spatial orbitals, i, j, k, l correspond to occupied orbitals, a, b, c, d correspond to virtual orbitals, and t, v, x, y correspond to active orbitals. Furthermore, we employ the ground-state one- and two-body reduced densities,

$$\gamma_{pq} = \sum_{\sigma} \langle \Psi_0 | \hat{a}_{q\sigma}^{\dagger} \hat{a}_{p\sigma} | \Psi_0 \rangle, \quad (\text{A1a})$$

$$\Gamma_{pqrs} = \sum_{\sigma\tau} \langle \Psi_0 | \hat{a}_{p\sigma}^{\dagger} \hat{a}_{r\tau}^{\dagger} \hat{a}_{s\tau} \hat{a}_{q\sigma} | \Psi_0 \rangle, \quad (\text{A1b})$$

and the transition density matrices

$$\gamma_{pq}^K = \sum_{\sigma} \langle \Psi_0 | \hat{a}_{q\sigma}^{\dagger} \hat{a}_{p\sigma} | \Psi_K \rangle, \quad (\text{A2a})$$

$$\Gamma_{pqrs}^K = \sum_{\sigma\tau} \langle \Psi_0 | \hat{a}_{p\sigma}^{\dagger} \hat{a}_{r\tau}^{\dagger} \hat{a}_{s\tau} \hat{a}_{q\sigma} | \Psi_K \rangle. \quad (\text{A2b})$$

Explicit expressions for the non-zero matrix elements can be simplified depending on the types of orbitals involved, giving expressions for the ground-state density matrices as

$$\gamma_{ij} = 2\delta_{ij} \quad (\text{A3})$$

and

$$\Gamma_{ijkl} = 4\delta_{ij}\delta_{kl} - 2\delta_{il}\delta_{kj}, \quad \Gamma_{ijtv} = 2\delta_{ij}\gamma_{vt}, \quad \text{and} \quad \Gamma_{ivtj} = -\delta_{ij}\gamma_{vt}. \quad (\text{A4})$$

where the purely active components γ_{tv} and Γ_{tvxy} cannot be simplified beyond Eq. A1. The only non-zero component of the one-body transition density matrix is γ_{tv}^K . In addition to the Γ_{tvxy}^K components, the non-zero terms of the two-body transition density matrix include

$$\Gamma_{ijtv}^K = 2\delta_{ij}\gamma_{vt}^K, \quad \text{and} \quad \Gamma_{ivtj}^K = -\delta_{ij}\gamma_{vt}^K. \quad (\text{A5})$$

2. Gradient terms

The gradient can be divided into the orbital components g^o and the CI components g^c that are defined in Eqs. (10a) and (10b), respectively. The CI components are given by the Hamiltonian matrix elements in the configuration space, that is

$$g_K^c = 2 \langle \Psi_0 | \hat{H} | \Psi_K \rangle. \quad (\text{A6})$$

The orbital components are given by

$$g_{mn}^o = \langle \Psi_0 | [\hat{H}, \hat{E}_{mn}] | \Psi_0 \rangle \quad (\text{A7})$$

where

$$\langle \Psi_0 | [\hat{H}, \hat{E}_{mn}] | \Psi_0 \rangle = \sum_p (h_{mp}\gamma_{pn} + \gamma_{np}h_{pm}) + \sum_{prs} [(pm|rs)\Gamma_{pnrs} + (mp|rs)\Gamma_{nprs}], \quad (\text{A8})$$

and we have introduced the singlet excitation operator

$$\hat{E}_{mn} = \sum_{\sigma \in \{\uparrow, \downarrow\}} \hat{a}_{m\sigma}^{\dagger} \hat{a}_{n\sigma} - \hat{a}_{n\sigma}^{\dagger} \hat{a}_{m\sigma} \quad (\text{A9})$$

with its anti-symmetrized variant $\hat{E}_{mn}^- - \hat{E}_{nm}^-$.

3. Hessian terms

Similarly, we can divide the Hessian \mathbf{Q} into three components: \mathbf{Q}^{cc} , \mathbf{Q}^{oo} and \mathbf{Q}^{oc} (where $H^{co} = (\mathbf{Q}^{oc})^\dagger$). The CI-CI components are given by the Hamiltonian matrix elements within the active configuration space shifted by the current energy E_0 , giving

$$Q_{K,L}^{cc} = 2 \langle \Psi_K | \hat{H} - E_0 | \Psi_L \rangle. \quad (\text{A10})$$

The off-diagonal components corresponding to the orbital-CI matrix elements are given by

$$Q_{mn,K}^{oc} = \langle \Psi_0 | [\hat{H}, \hat{E}_{mn}^-] | \Psi_K \rangle \quad (\text{A11})$$

where the constituent transition matrix elements are computed as

$$\langle \Psi_K | [\hat{H}, \hat{E}_{mn}] | \Psi_0 \rangle = \sum_p (h_{mp} \gamma_{pn}^K + \gamma_{np}^K h_{pm}) + \sum_{prs} [(pm|rs) \Gamma_{pnrs}^K + (mp|rs) \Gamma_{nprs}^K]. \quad (\text{A12})$$

The final orbital-orbital term is given by

$$Q_{pq,rs}^{oo} = \frac{1}{2} (\langle \Psi_0 | [[\hat{H}, \hat{E}_{pq}^-], \hat{E}_{rs}^-] | \Psi_0 \rangle + \langle \Psi_0 | [[\hat{H}, \hat{E}_{rs}^-], \hat{E}_{pq}^-] | \Psi_0 \rangle). \quad (\text{A13})$$

While a full derivation is mathematically involved, the non-redundant blocks are:

- Virtual-Core,Virtual-Core:

$$Q_{ai,bj}^{oo} = 4[4(ai|bj) - (ab|ij) - (aj|bi)] + 4\delta_{ij}(F_{ab}^C + F_{ab}^A) - 4\delta_{ab}(F_{ij}^C + F_{ij}^A) \quad (\text{A14})$$

- Virtual-Core,Virtual-Active:

$$Q_{ai,bt}^{oo} = 2 \sum_v \gamma_{tv} [4(ai|bv) - (av|bi) - (ab|vi)] - \delta_{ab} \left(\sum_v \gamma_{tv} F_{iv}^C + 2(F_{ti}^C + F_{ti}^A) + \sum_{vxy} \Gamma_{tvxy}(vi|xy) \right) \quad (\text{A15})$$

- Virtual-Core,Active-Core:

$$Q_{ai,tj}^{oo} = 2 \sum_v (2\delta_{tv} - \gamma_{tv}) [4(ai|vj) - (av|ji) - (aj|vi)] - \delta_{ij} \left(\sum_v \gamma_{tv} F_{av}^C - 4(F_{at}^C + F_{at}^A) + \sum_{vxy} \Gamma_{tvxy}(av|xy) \right) \quad (\text{A16})$$

- Virtual-Active,Virtual-Active:

$$Q_{at,bu}^{oo} = 2 \sum_{vx} \left(\Gamma_{tvx}(ab|vx) + (\Gamma_{txvu} + \Gamma_{txuv})(ax|bv) \right) - \delta_{ab} \left(\sum_v (\gamma_{tv} F_{uv}^C + \gamma_{uv} F_{tv}^C) + \sum_{vxy} (\Gamma_{tvxy}(uv|xy) + \Gamma_{uvxy}(tv|xy)) \right) + 2\gamma_{tu} F_{ab}^C \quad (\text{A17})$$

- Active-Core,Virtual-Active:

$$Q_{ti,au}^{oo} = -2 \sum_{vx} \left(\Gamma_{tvx}(ai|vx) + (\Gamma_{tvux} + \Gamma_{tvxa})(ax|vi) \right) + 2 \sum_v \gamma_{uv} \left(4(av|ti) - (ai|tv) - (at|vi) \right) - 2\gamma_{tu} F_{ia}^C + \delta_{tu}(F_{ai}^C + F_{ai}^A) \quad (\text{A18})$$

- Active-Core,Active-Core:

$$\begin{aligned} G_{ti,uj} &= 2 \sum_v (\delta_{tv} - \gamma_{tv}) \left(4(vi|uj) - (ui|vj) - (uv|ij) \right) + 2 \sum_{vx} \left(\Gamma_{tvx}(vx|ij) + (\Gamma_{uxvt} + \Gamma_{uxtv})(vi|xj) \right) \\ &\quad + 2\gamma_{tu} F_{ij}^C - 2\delta_{ij} \left(\sum_{vxy} \Gamma_{tvxy}(uv|xy) + \sum_v \gamma_{uv} F_{tv}^C \right) + 4\delta_{ij}(F_{tu}^C + F_{tu}^A) - 4\delta_{tu}(F_{ij}^C + F_{ij}^A) \\ Q_{ti,uj}^{oo} &= \frac{1}{2} (G_{ti,uj} + G_{uj,ti}). \end{aligned} \quad (\text{A19})$$

Here, we have introduced the inactive (core) and active Fock matrices⁹²

$$F_{mn}^C = h_{mn} + \sum_i [2(mn|ii) - (mi|in)] \quad \text{and} \quad F_{mn}^A = \sum_{tv} \gamma_{tv} [(mn|tv) - \frac{1}{2}(mv|tn)]. \quad (\text{A20})$$

B. Eigenvector-following for saddle point optimisation

We employ the eigenvector-following technique to target stationary points with an arbitrary Hessian index. While Section 6.2.1 of Ref. 106, and references therein, describe this method in detail, here we summarise the salient points for completeness and provide the details of our particular implementation.

Eigenvector-following works in the eigenbasis for the Hessian matrix \mathbf{Q} with eigenvalues ϵ_μ . In this basis, the components of the Newton–Raphson step $\mathbf{x} = -\mathbf{Q}^{-1}\mathbf{g}$, with gradient \mathbf{g} , and the change in energy ΔV are given by

$$x_{\text{NR},\mu} = -\frac{g_\mu}{\epsilon_\mu} \quad \text{and} \quad \Delta V_{\text{NR}} = -\sum_\mu \frac{|g_\mu|^2}{2\epsilon_\mu}. \quad (\text{B1})$$

Contributions with $\epsilon_\mu > 0$ or $\epsilon_\mu < 0$ lower or raise the energy, respectively. To drive the optimisation towards a particular type of Hessian index, eigenvector-following artificially modifies the sign of these components. In particular, the components of the quasi-Newton eigenvector-following step are defined as

$$x_{\text{QN},\mu} = \frac{\pm 2g_\mu}{|\epsilon_\mu| \left(1 + \sqrt{1 + |2g_\mu/\epsilon_\mu|^2} \right)}, \quad (\text{B2})$$

where a positive or negative step gives an uphill or downhill step, respectively. This expression reduces to the Newton–Raphson step in the $g_\mu \rightarrow 0$ limit and can be understood by imposing constraints on each component using Lagrange multipliers. When an index- n saddle point is targeted in this work, the components corresponding to the lowest n eigenvalues of the Hessian are chosen to be downhill directions.

Furthermore, we employ a dogleg trust radius technique to control the step length and improve the local convergence behaviour. A trust radius method works by defining a circular region with radius ρ around the current point in which a quadratic approximation to the objective function is considered to be accurate. The next step is chosen by optimising the objective function within this trust region, known as the sub-problem. In practice, approximate solutions to this sub-problem are required, and we employ the dogleg method (see Section 4.1 of Ref. 108). This method requires an analogue of the steepest descent direction for saddle point optimisation. To target saddle points, we define this “steepest descent” step as

$$x_{\text{SD},\mu} = \pm g_\mu, \quad (\text{B3})$$

where the positive and negative sign for each component are chosen in the same way as the quasi-Newton step [Eq. (B2)]. Defining an unconstrained step which optimises the energy along the steepest descent direction as

$$\mathbf{x}_U = -\frac{\mathbf{g}^\dagger \mathbf{x}_{\text{SD}}}{\mathbf{x}_{\text{SD}}^\dagger \mathbf{Q} \mathbf{x}_{\text{SD}}} \mathbf{x}_{\text{SD}}, \quad (\text{B4})$$

and using the eigenvector-following quasi-Newton step \mathbf{x}_{QN} , the optimal dogleg step \mathbf{x} is then given by

$$\mathbf{x} = \begin{cases} \mathbf{x}_{\text{QN}} & \text{if } |\mathbf{x}_{\text{QN}}| \leq \rho \\ \frac{\rho}{|\mathbf{x}_U|} \mathbf{x}_U & \text{if } |\mathbf{x}_U| \geq \rho \\ \mathbf{x}_U + \tau(\mathbf{x}_{\text{QN}} - \mathbf{x}_U) & \text{otherwise} \end{cases} \quad (\text{B5})$$

where

$$\tau = \frac{-b + \sqrt{b^2 - 4ac}}{2a}, \quad a = |\mathbf{x}_{\text{QN}} - \mathbf{x}_U|^2, \quad b = 2\mathbf{x}_U \cdot (\mathbf{x}_{\text{QN}} - \mathbf{x}_U), \quad c = |\mathbf{x}_U|^2 - \rho^2. \quad (\text{B6})$$

The trust radius is then updated by comparing the ratio of the actual energy change ΔE to that predicted by the quadratic model ΔE_{model} . The trust radius is halved for $\Delta E/\Delta E_{\text{model}} < 0.25$, and doubled if $\Delta E/\Delta E_{\text{model}} > 0.75$ and $|\mathbf{x}_{\text{DL}}| = \rho$. Otherwise, the trust radius is deemed to not be interfering with the optimisation and is left unchanged. Finally, a step is rejected if ΔE and ΔE_{model} have different signs. We find that an initial trust radius of 0.15 provides adequate optimisation behaviour.

C. Mode-controlled Newton–Raphson optimisation

Once a stationary point has been identified, it can be followed along a potential energy surface by using the old orbital and CI coefficients as a guess at the new geometry. Since the Hessian index can change at different geometries, we use a standard

Newton–Raphson optimisation to perform this optimisation. The Newton–Raphson step is identified by solving a quadratic Taylor series expansion to the energy around a given point, giving

$$\mathbf{x}_{\text{NR}} = -\mathbf{Q}^{-1}\mathbf{g} \quad (\text{C1})$$

for the gradient \mathbf{g} and Hessian matrix of second derivatives \mathbf{Q} . The dogleg method (described in Appendix B) cannot be used as there is no way of defining a “steepest descent” step for saddle point optimisation without knowing the target Hessian index. Instead, we simply truncate the components of \mathbf{x}_{NR} depending on their magnitude along each eigen-direction of the \mathbf{Q} , giving

$$x_\mu = \min(|x_{\text{NR},\mu}|, \rho) \frac{x_{\text{NR},\mu}}{|x_{\text{NR},\mu}|}. \quad (\text{C2})$$

The trust radius ρ is then updated using the same strategy described in Appendix B. Similar mode-controlled Newton–Raphson optimisation algorithms have been reported multiple times in the past.^{2–4,107}